EUROPEAN ORGANIZATION FOR NUCLEAR RESEARCH

CERN–EP/2002–087
November 7, 2002

Performance of the ATLAS electromagnetic calorimeter barrel module 0

The ATLAS Electromagnetic Liquid Argon Calorimeter Group*

ABSTRACT

The construction and performance of the barrel pre-series module 0 of the future ATLAS electromagnetic calorimeter at the LHC is described. The signal reconstruction and performance of ATLAS-like electronics has been studied. The signal to noise ratio for muons has been found to be 7.11±0.07. An energy resolution of better than $9.5\% \cdot \mathrm{GeV}^{1/2}/\sqrt{E}$ (sampling term) has been obtained with electron beams of up to 245 GeV. The uniformity of the response to electrons in an area of $\Delta\eta \times \Delta\phi = 1.2 \times 0.075$ has been measured to be better than 0.8%.

(Submitted to Nucl. Instr. and Meth. A)

*) See next pages for the list of authors.

B. Aubert, J. Ballansat, A. Bazan, B. Beaugiraud, J. Boniface, F. Chollet, J. Colas, P. Delebecque, L. Di Ciaccio, N. Dumont-Dayot, M. El Kacimi[a], O. Gaumer, P. Ghez, C. Girard, M. Gouanère, H. Kambara, A. Jérémie, S. Jézéquel, R. Lafaye, T. Leflour, C. Le Maner, J. Lesueur, N. Massol, M. Moynot, L. Neukermans, P. Perrodo, G. Perrot, L. Poggioli, J. Prast, H. Przysiezniak, X. Riccadona, G. Sauvage, J. Thion, I. Wingerter-Seez, R. Zitoun,Y. Zolnierowski

Laboratoire de Physique de Particules (LAPP), IN2P3-CNRS, F-74019 Annecy-le-Vieux Cedex, France.

H. Chen, M. Citterio[b], J. Farrell, H. Gordon, B. Hackenburg, A. Hoffman, J. Kierstead, F. Lanni, M. Leite[c], D. Lissauer, H. Ma, D. Makowiecki, V. Radeka, D. Rahm, S. Rajagopalan, S. Rescia, I. Stumer, H. Takai, K. Yip

Brookhaven National Laboratory (BNL), Upton, NY 11973-5000, USA.

D. Benchekroun, C. Driouichi, A. Hoummada, M. Hakimi

Faculté des Sciences Aïn Chock, Casablanca, Morocco.

R. Stroynowski, J. Ye

Southern Methodist University, Dallas, Texas 75275-0175, USA.

J. Beck Hansen, A. Belymam, J. Bremer, J.L. Chevalley, P. Fassnacht, F. Gianotti, L. Hervas, C.P. Marin, P. Pailler, P. Schilly W. Seidl, J. Vossebeld, V. Vuillemin

European Laboratory for Particle Physics (CERN), CH-1211 Geneva 23, Switzerland.

A. Clark, I. Efthymiopoulos, L. Moneta

Université de Genève, CH-1211 Geneva 4, Switzerland.

B. Belhorma, J. Collot, P. de Saintignon, D. Dzahini, A. Ferrari, M.L. Gallin-Martel, J.Y. Hostachy, P. Martin, J.F. Muraz, F. Ohlsson-Malek, S. Saboumazrag

Institut des Sciences Nucléaires, Université Joseph Fourier, IN2P3-CNRS, F-38026 Grenoble, France.

J. Ban, N. Cartiglia[d], H. Cunitz, J. Dodd, A. Gara, M. Leltchouk, S. Negroni, J.A. Parsons, M. Seman, S. Simion, W. Sippach, W. Willis

Nevis Laboratories, Columbia University, Irvington, NY 10533, USA.

F. Barreiro, G. Garcia[e], L. Labarga, S. Rodier[f], J. del Peso

Physics Department, Universidad Autónoma de Madrid, Spain.

C. Alexa[g], P. Barrillon, C. Benchouk, A. Chekhtman, B Dinkespiler, F. Djama, P.Y. Duval, F. Henry-couannier, L. Hinz[h], M. Jevaud, P. Karst, A. Le Van Suu, L. Martin, O. Martin, A. Mirea[i], E. Monnier, E. Nagy, D. Nicod, C. Olivier, P. Pralavorio, B. Repetti, M. Raymond, D. Sauvage[j], S. Tisserant, J. Toth[k], M. Wielers[l]

Centre de Physique des Particules de Marseille, Univ. Méditerranée, IN2P3-CNRS, F-13288 Marseille, France.

G. Battistoni, W. Bonivento[m], L. Carminati, D. Cavalli, G. Costa, M. Delmastro, M. Fanti, L. Mandelli, M. Mazzanti, L. Perini, S. Resconi, G. F. Tartarelli

Dipartimento di Fisica dell'Universitá di Milano and INFN, I-20133 Milano, Italy.

V. Aulchenko, V. Kazanin, G. Kolachev[j], V. Malyshev, A. Maslennikov, G. Pospelov, R. Snopkov, A. Shousharo, A. Talyshev, Yu. Tikhonov

Budker Institute of Nuclear Physics, RU-630090 Novosibirsk, Russia.

E. Augé, C. Bourdarios, D. Breton, P. Cros, C. de La Taille, I. Falleau, D. Fournier, G. Guilhem, S. Hassani, Y. Jacquier, K. Kordas[i], G. Macé, B. Merkel, J.M. Noppe, G. Parrour, P. Pétroff, P. Puzo, J.P. Richer[n], D. Rousseau, N. Seguin-Moreau, L. Serin, V. Tocut, J.J. Veillet, D. Zerwas

Laboratoire de l'Accélérateur Linéaire, Université de Paris-Sud, IN2P3-CNRS, F-91898 Orsay Cedex, France.

F. Astesan, W. Bertoli, A. Camard, B. Canton, S. Fichet, F. Hubaut, D. Imbault, D. Lacour, B. Laforge, O. Le Dortz, D. Martin, I. Nikolic-Audit, F. Orsini, F. Rossel, P. Schwemling

Laboratoire de Physique Nucléaire et de Hautes Energies, Université Paris VI et VII, IN2P3-CNRS, F-Paris, France.

W. Cleland, J. McDonald

Department of Physics and Astronomy, University of Pittsburgh, Pittsburgh, PA 15260, USA.

E.M. Abouelouafa, A. Ben Mansour, R. Cherkaoui, Y. El Mouahhidi, H. Ghazlane and A. Idrissi

Faculté des Sciences and Centre National de l'Énergie des Sciences et des Techniques Nucléaires, Rabat, Morocco.

J. Belorgey, R. Bernard, M. Chalifour, A. Le Coroller, J. Ernwein, B. Mansoulié, J.F. Renardy, J. Schwindling, J.-P. Taguet, J. Teiger

CEA, DAPNIA/Service de Physique des Particules, CE-Saclay, F-91191 Gif-sur-Yvette Cedex, France.

C. Clément, B. Lund-Jensen, J. Lundqvist, L. Megner, M. Pearce, S. Rydstrom

Royal Institute of Technology, Stockholm, Sweden.

J. Egdemir, R. Engelmann, J. Hoffman, R. McCarthy, M. Rijssenbeek, J. Steffens

State University of New York, Stony Brook, New York 11794, USA.

(a) Visitor from LPHEA, FSSM-Marrakech (Morroco).
(b) Now at Dipartimento di Fisica dell'Universitá di Milano and INFN, I-20133 Milano, Italy.
(c) Also at Sao Paulo University. Work partially supported by FAPESP/ Sao Paulo (Brazil).
(d) Now at Dipartimento di Fisica dell'Universitá di Torino, I-10125 Torino, Italy.
(e) Now at "Instituto Nicolas Cabrera", U.A.M. Madrid.
(f) Supported by the TMR-M Curie Programme, Brussels.
(g) Also at Institute of Atomics Physics, National Institute for Physics and Nuclear Engineering IFIN-HH, Bucharest, Romania.
(h) Now at Université de Lausanne, Faculté des Sciences, Institut de Physique des Hautes Energies.
(i) Now at University of Toronto, Dept. of Physics, Toronto, Canada.
(j) Deceased.
(k) Also at KFKI, Budapest, Hungary. Supported by the MAE, France, the HNCfTD (Contract F15-00) and the Hungarian OTKA (Contract T037350).
(l) Now at TRIUMF laboratory, Vancouver, Canada.
(m) Also at INFN, Sezione di Cagliari, Italy.
(n) Now at Institut des Sciences Nucléaires, Université Joseph Fourier.

1 Introduction

The electromagnetic calorimeter of the ATLAS experiment at CERN's future proton-proton collider, the LHC, is a lead-liquid argon sampling calorimeter with accordion shaped absorbers and electrodes. Liquid argon calorimetry has been chosen because of its intrinsic linear behavior, stability of the response and radiation tolerance.

Results of R&D work were reported in [1, 2, 3, 4]. In this paper the construction and tests of the pre-series module 0 of the barrel calorimeter are described. The module has the same dimensions as the 32 modules of the future barrel calorimeter of ATLAS. As a result of extensive Monte Carlo optimizations [5], in particular the study of γ/π^0 separation, the granularity of the presampler and of the calorimeter module was changed with respect to the preshower detector and the prototype described in [4]. The granularity of the presampler is coarser, while the granularity in η of the first calorimeter sampling is finer and its depth is decreased. In addition the length (η) of the module is covered with only two electrodes instead of five to minimize the dead zones between electrodes. The module 0 electronics have the full functionality required for ATLAS, with the exception that not all components are resistant to the high radiation levels expected at the LHC.

The module was the last prototype to be tested before the production of the series modules of the ATLAS barrel calorimeter. Its purpose was to validate the construction chain and to study the electronics performance. The module was exposed to electron and muon beams in the North Area at CERN's SPS in order to study the energy resolution and the uniformity of the calorimeter response.

The paper is organized as follows. In Sections 2 and 3 the construction and quality control of the calorimeter module and of the presampler are discussed. The electronics chain is then described (Section 4), followed by the description of the beam setup (Section 5). The modeling of the detector response is described in Section 6, the signal reconstruction and performance are discussed in Section 7. The response to muons and electrons is discussed in Sections 8 and 9 respectively, followed by conclusions and prospects.

2 Calorimeter Module 0 Construction

The ATLAS barrel electromagnetic calorimeter, described in detail in [6], is made of two half-barrels, centered around the z-axis (ATLAS beam axis). One half-barrel covers z$>$ 0 (pseudorapidity $\eta > 0$) and the other one z$<$ 0 ($\eta < 0$), from $|\eta| = 0$ to $|\eta| = 1.475$; the length of each half-barrel is 3.2 m, the inner and outer diameters are about 2.8 m and 4 m respectively. A half-barrel is made of 1024 accordion shaped absorbers, interleaved with readout electrodes.

The electrodes are kept in the middle of the gap by spacers made from strips of honeycomb material, joined into an accordion shaped sheet by resin impregnated threads. The drift gap on each side of the electrode is 2.1 mm, which corresponds to a total drift time of about 450 ns for an operating voltage of 2000 V.

Once assembled, there is no discontinuity along the azimuthal angle ϕ; but for ease of construction, a half-barrel is divided into 16 modules. The total thickness of a module is at least 22 radiation lengths (X_0), increasing from $22X_0$ to $30X_0$ between $|\eta| = 0$ and $|\eta| = 0.8$, and from $24X_0$ to $33X_0$ between $|\eta| = 0.8$ and $|\eta| = 1.3$.

A module, shown in Figure 1, has three compartments in depth (front, middle, back). The readout granularity of the different compartments is shown in Table 1 for $\eta < 1.3$ (for module 0 we set $\eta > 0$ and approximate values will be given for ϕ instead of the exact ones, e.g., 0.025 instead of $\pi/128$). In total there are 3428 readout cells per module.

2.1 Absorbers

The absorbers are made of lead sheets (thickness 1.53 mm for $\eta < 0.8$, 1.13 mm for $\eta > 0.8$), glued between two 0.2 mm thick stainless steel sheets by resin-impregnated glass fiber fabric. The fiber fabric compensates for the difference in thickness of the two types of lead plates so that the nominal thickness of an absorber is 2.2 mm.

A local non-uniformity of the thickness of the lead plates induces variations of the calorimeter response [4, 7]. Its effect on the constant term of the energy resolution can be approximated by the relative rms of the distribution of the sliding mean of the thickness of five consecutive lead plates multiplied by one-half [8, 9]. In order to keep the constant term induced by inhomogeneities below 0.3%, the lead thickness has been measured by radiography (using a setup developed with the help of CEA-DAMRI) during the cold rolling process at the factory. This allowed for fast machine adjustments and rejection of lead sheet sections out of tolerance. The precision of the lead thickness obtained, in an acceptance window of 60 μm, is better than 0.8% (rms) for $\eta < 0.8$ (0.6% for $\eta > 0.8$). The production procedure improves significantly the precision attainable by standard cold rolling alone. Plates were cut out of these rolls

and stored. Each plate was then measured by ultrasound to get a detailed thickness map [10]. A sorting algorithm was used to match lead plates in order to compensate for local non-uniformities. Deduced from the relative rms of the sliding mean thickness, a contribution to the constant term of 0.12% ($\eta < 0.8$) and 0.18% ($\eta > 0.8$) is expected.

The absorbers are formed into an accordion shape as described in [6]. After the gluing cycle, they are equipped with precisely machined G10 bars (maximal dispersion of ± 80 μm for groups of 16 bars in Rϕ). The final geometry is measured with a 3D coordinate machine to give feedback on the bending machine stability [11]. The dispersions of the opening half-angles, varying from 46.5° at small radius to 34° at large radius, are of the order of 0.15° to 0.5°. For the straight section lengths a dispersion of 0.02 mm is obtained, while for the distance between the precision bars the dispersion is 0.15 mm. The thickness profile are shown in Figure 2 for the raw and sliding averages. The rms of the absorber thickness distribution is 19 μm (13 μm) for the raw (sliding average) thicknesses.

2.2 Electrodes

The readout electrodes, 275 μm thick, consist of three conductive copper layers separated by insulating polyimide sheets. The two outer layers are at the high voltage potential, the inner one is used for reading out the signal through capacitive coupling. The granularity of the calorimeter in η and in depth is obtained by etched patterns on the different layers. Each gap between two absorbers is equipped with two electrodes: type A ($\eta < 0.8$) and type B ($\eta > 0.8$).

The main difference with respect to previous prototypes is the use of large size electrodes. Before bending the electrodes are ~ 1.8 m $\times$ 0.8 m.

Copper clad polyimide (single-sided with pre-cured glue coating and double-sided) laminate is used to make the three layered circuits. The base polyimide is (Dupont's) Kapton-E type, which has a thermal expansion coefficient close to that of copper. This leads to minimal geometrical deformations relative to the absorber system at cryogenic temperatures. The HV protection resistor pads are silk screened with one component epoxy based resistive ink[1)]. Nominal resistivity is 1 MΩ/square (at room temperature) [12]. The pads were measured individually for each electrode on dedicated testbenches. Each signal path and HV connection is equipped with one or more gold plated female contacts, directly crimped (and soldered) on copper pads on the circuit. The electrodes are equipped with springs for the ground return connection between the electrode and absorber.

Several important production parameters were obtained with the pre-series electrode production for this module 0. The global dimensions of etched images with respect to films are typically precise to ± 0.2 mm. The copper etching is precise and well controlled over the whole area. For most electrodes the alignment between layers is better than ± 0.4 mm, less than the ± 0.5 mm left as separation between cells. This has been checked visually for all electrodes.

On the other hand several defects and problems were encountered. The film dimensions, not controlled before usage, were ~ 0.7 mm smaller than design. About one-third of the electrodes had to be discarded, as they did not tolerate the curing cycle for the resistive ink due to bad gluing of the laminates. For about half of the remaining electrodes the curing cycle temperature had to be lowered, yielding large values and a large dispersion of the serigraphied resistors. On about 20 electrodes, output traces (in the signal layer) were damaged when etching the outer layers leading to a few dead cells in the front section. For part of the electrodes, the positioning of the crimps was done manually resulting in a misalignment of connectors up to ~ 1 mm between different gaps. One quarter of the electrodes suffered from positioning defects between image and the stacking holes (used to fix the electrodes to the G10 bar of the absorber). Most of these defects were understood and were due mostly to the lack of proper tooling at that time.

The electrodes were bent to accordion shape with the machine described in detail in [6]. All resistors and blocking capacitances were measured with a semi-automatic setup (low voltage test). A high voltage test was performed by measuring the leakage current between the electrode outer layers kept at 2000 V and the inner layer connected to ground. The standard test had a duration of one hour. Both tests were performed before and after bending [13, 14]. Depending on the degree of curing of the resistive ink, some electrodes showed damaged resistors after bending the flat circuits. This was seen in particular for resistors closer than 10 mm to the peak of the bend (see Figure 3).

In a module, 64 A- and 64 B-electrodes are needed. In total 150 electrodes were produced[2)], of which 49 were unusable. 31 A-electrodes out of 47 and 22 B-electrodes out of 54 had high resistance values with a large dispersion. The experience gained by the factories in the pre-series production for module 0 and additional R&D and significant design changes have improved the situation and led to the

[1)] DL1216 ESL.

[2)] CICOREL SA, 8 route de l'Europe, CH-2017 Boudry and MCB Industrie, 107-11 rue du Moulin Sarrazin, F-95100 Argenteuil.

solution of most of the problems described in this Section. The efficiency in the series production has been greatly improved.

2.3 Module Assembly

With the limited number of electrodes available, only the central region of the module could be equipped with electrodes with normal resistance values. This region corresponds to $0.2 < \phi < 0.3$ in the A electrodes and $0.1 < \phi < 0.3$ in the B electrodes. The other electrodes were placed around these central regions, so that for $\eta < 0.8$ the region $0.125 < \phi < 0.4$ and for $\eta > 0.8$ the region $0.025 < \phi < 0.35$ was equipped.

The geometry of the module is defined by the external and internal G10 bars. Their prismatic shape is such that a stack of 64 absorbers makes a wedge with an angle of 22.5°. The outer bars are screwed on support stainless steel ring pieces which define the external radius of the module.

The stacking is done on a rotating jig in a clean room (class ISO 8) with the relative humidity controlled to $50\% \pm 5\%$. The module is stacked in the horizontal position, but tightening the absorber to the preceding one and to the ring piece is done in a vertical position to avoid sagging of the absorbers.

The stacking procedure is the following: the set of 6 ring-pieces fixed to its module assembly backbone is aligned on the module assembly jig. Then the first absorber is fixed in place with references in all axes (to about 0.1 mm). A first spacer plane, the electrode plane, a second spacer plane and a new absorber are stacked. Dowel pins position the electrode accurately in r and z with respect to the preceding absorber; other dowel pins position the new absorber in r, its z position being defined by a stop at z= 0. After rotating to the vertical position, the new absorber is pressed against the preceding one with pneumatic jacks acting on the outer and inner G10 bars. The screws linking the absorber to the preceding one and to the ring-piece are tightened to the desired torque. This stacking sequence is repeated 64 times. Typically four absorbers can be stacked per day.

Regularly, every 2 or 4 detector gaps, two electrical tests are performed. A low frequency signal (1 to 6 Hz) is injected on the HV lines and the induced signals on the signal outputs are recorded [15]. This test checks the continuity of the electrical circuit and the electrode connections including the high voltage distribution. Then a HV test is performed : 1800 V is applied to the electrodes and the leakage currents are recorded.

Every 4 gaps, the thickness of the stack is measured at the inner and outer absorber G10 bars and at several locations in z in order to control the final dimension of the module and also the thickness of the gaps. The imperfect shape, due to a deviation from the nominal folding angle of the bent electrodes of module 0, introduced a deformation of the module geometry with as consequence a small over-thickness at the inner and external radii. The evolution of the module over-thickness at the external radius is shown in Figure 4. After the last absorber is stacked, an increase of about 0.2 mm is observed.

The aim was to obtain an argon gap dispersion of the order of 50 μm to keep the contribution to the constant term of the energy resolution below 0.15%. In module 0, the gap capacitances were measured and their dispersion translated into a dispersion of the gap thickness of 82 μm.

2.4 Cold Electronics and Cabling

The front section is read out at the inner radius, whereas middle and back sections are read out from the back (outer radius). Summing boards are connected to the electrode connectors to group the signals in ϕ to the desired readout granularity (Table 1): 16 electrodes are grouped into one cell for the front section, 4 for the middle and back sections. The boards are 10 layer PCBs with 15 Ω strip-lines whose lengths are equalized in ϕ in order to ensure a uniform inductance.

The summing boards are connected to the motherboards. These boards route the outputs to the readout cables through "low profile" connectors and include precision injection resistors (0.1% and 70 ppm/°C) for the calibration system. The readout cables are miniature polyimide coaxial cables[3] [16]: 25 Ω for the back and middle sections, 50 Ω for the front section to optimize the noise contribution. The readout cables are grouped in bundles of 64 channels and connected at the end of the module to high density μD 100 connectors, fitting 64 channels and 32 ground connections in a 10×30 mm^2 area. The connectors are fixed on a patch panel.

The high voltage is supplied to electrodes through boards connected at the back of the module. The two sides of the electrodes are fed by different high voltage lines, thus providing a safety margin. In η the module is divided into seven HV sectors of $\Delta\eta = 0.2$; in ϕ the HV sector size is $\Delta\phi = 0.2$.

After cabling, the HV connectivity is checked with a low frequency test. Each cell is pulsed and its signal is recorded. A high voltage test is then performed. All tests are performed at room temperature.

[3] AXON CABLE SA, Route de Chalons-en-Champagne, 51210 Montmirail, France.

3 Presampler Construction

The liquid argon barrel presampler [17] is placed in front of the electromagnetic calorimeter inside the cryostat. In ATLAS it will consist of 64 sectors. The presampler's dimensions are defined by an envelope that for a half barrel is a 3.1 m long, 23 mm thick annulus with a diameter of about 2.9 m. Each sector provides coverage in η from 0 to 1.52 and covers a region of $\Delta\phi = 0.2$. The signal is sampled in a thin active layer of 11 mm of liquid argon with a readout cell granularity of $\Delta\eta \times \Delta\phi = 0.025 \times 0.1$.

Each sector is composed of eight modules of unequal lengths (constant $\Delta\eta$) held together by 3.1 m long FR4 bars, as shown in figure 5. A module covers a region of 0.2×0.2 in (η, ϕ), with the exception of the modules located at the ends of the barrel, for which the η coverage is reduced to 0.12.

The electrodes are perpendicular to the longitudinal axis except for the electrodes of the type 1 and 2 modules (the closest to the barrel center) which are slanted in order to keep a triangular shape for the signal response [18]. They are separated by ~ 2 mm liquid argon gaps and operated at a fixed high voltage of 2 kV. There are 2 kinds of electrodes: cathodes which are (270 ± 30) μm thick double sided boards; and anodes which are ($330\pm^{30}_{40}$) μm thick 3-layered boards. The 2 kV potential is applied to the external anode layers and the signal is read out through capacitive coupling to the central anode layer. Anode quality assurance tests include measurements of (a) values of the protective resistors soldered on the anodes, (b) capacitance of the electrodes and (c) leakage current obtained with an applied potential of 3 kV [19]. The number of electrodes per module type varies in order to keep the granularity and the liquid argon gap approximately constant. Readout cells of the required granularity are obtained by ganging the appropriate number of electrodes in the longitudinal direction on the modules themselves. In the ϕ-direction, each anode is subdivided into two compartments with $\Delta\phi = 0.1$ by etching.

The assembly procedure is the following: electrodes are first positioned in a jig of precision shims. Glass-epoxy plates covered with epoxy pre-impregnated[4)] foils are then applied to the top and bottom edges of the electrodes. During the curing cycle, pressure is applied by tightening screws mounted on the jig.

Eight different types of motherboards, with five printed circuit layers, are placed on their respective modules and collect signals from the readout cells. These boards are equipped with a set of accurate surface mounted resistors (see Section 2.4) for the injection of calibration pulses.

The signal cables, the same as those described in Section 2.4, are soldered onto the mother boards and grouped. There are eight high voltage channels per sector. The voltage in a region of (η,ϕ) of 0.4×0.2 is supplied by two lines connected to the two HV-layers of the anode, each of them connected to the odd and even HV-layers of the anode thus ensuring a safety margin.

Each sector is checked on a test-bench at low temperature (liquid nitrogen). A high voltage test is performed and the response of each channel is studied (noise and signal). The electrical connections are verified by connecting the HV inputs to a low voltage and low frequency sinusoidal signal.

4 Front End Electronics

The calorimeter signals are brought from the calorimeter module's patch panel (see Section 2) to the cold flange of the feedthrough. In the flange, high density ceramic pin carriers (2.54 mm pitch) operate the transition liquid argon-vacuum and vacuum-air. The ground return is brought through the bulk of the flange via gold-plated ground springs. A 35 Ω strip-line (40 cm long) cable connects the cold flange to the warm flange in the feedthrough vacuum and an additional 35 Ω strip-line (also 40 cm) cable connects the warm flange to the base-plane of the front end crate.

The crate houses (see Figure 6) the Front End Boards (FEB), which amplify, shape, store the signal during the trigger latency and then digitize the selected signals. The FEBs provide virtually dead-time free operation up to 75 kHz trigger rate. The crate also houses the calibration boards (CALIB), which generate high precision calibration pulses. These two types of boards fulfill the requirements of ATLAS in terms of dynamic range, noise, density, power, dimensions except for the radiation hardness. The boards are connected to the power bus by combs. They are water cooled with cooling plates mounted on each board. Underpressured water (18°C) is supplied via a manifold attached to the crate.

All the parameters necessary to operate the FEB and CALIB are downloaded through a custom serial link (SPAC [20]) derived from I^2C[5)], running at 10 MHz. A dedicated VME-based TTC (Trigger Timing Control) system was developed to distribute the 40 MHz clock and trigger signals and provide programmable delays [21] to make timing adjustments.

[4)] Prepreg 5512-18-08-50/120, manufactured by CTMI, Le Séré 38840, La Sone, France.

[5)] I^2C bus specifications patented by Philips Semiconductors.

4.1 Front End Boards

The FEB treats 128 channels in 16 groups of 8 channels. Each block includes: 2 four-channel preamplifiers, 2 four-channel shapers, 2 twelve-channel analog memories or SCA (Switched Capacitor Arrays) and one 12-bit ADC running at 5 MHz.

The preamplifiers are of "current sensitive" type to provide fast signals over the large dynamic range needed for operation at the LHC. The preamplifier is realized as a hybrid circuit, housing 4 channels in an area of 10 cm^2 [22]. It is characterized by the input impedance and its transimpedance (R_f). Three types of preamplifiers are used, one for the 50 Ω presampler and strip sections with a transimpedance of 3 kΩ for a dynamic range of 1 mA. The two others are used for the 25 Ω middle and back section with $R_f = 1$ kΩ and $R_f = 500\ \Omega$ corresponding to a dynamic range of 5 mA and 10 mA respectively.

The preamplifier architecture is an active common base configuration for high speed, with feedback on the base to raise the input impedance to 25 or 50 Ω. The input impedance exhibits very low base resistance ($R_{BB'} \simeq 4\ \Omega$). It is operated at 5 mA collector current to reach an overall noise performance of e_n=0.4 nV/$\sqrt{\text{Hz}}$; i_n=6 pA/$\sqrt{\text{Hz}}$. A protection network is added in front of the preamplifier in order to withstand potential HV sparks in the detector gaps. The preamplifiers have been produced, tested and screened in order to guarantee the uniformity requirements reported in [6].

The shaper chip [23], realized in austriamicrosystems'[6] 1.2μm BiCMOS technology, is located immediately after the preamplifier. The chip has a CR-RC^2 architecture with a time constant of $\tau = 13$ ns, optimized for the total noise at high luminosity at the LHC [24]. One differentiation removes the long trailing tail of the LAr signal and two integrations limit the useful bandwidth and reduce electronics noise. The shaper splits the 16 bit dynamic range in three linear scales of 12 bits each, i.e. there are twelve output channels per shaper. The noise of the high, medium and low gain scale, measured on a dedicated test-bench, is 850 μV, 390 μV and 250 μV respectively. The integral non-linearity was measured to be better than 0.2%.

After shaping the signal is sampled at 40 MHz and stored in the SCA chip (HP 1.2 μm technology). The chip contains 16 analog channels with 144 storage cells each: 12 of the channels (four channels in three gains) are used to store the signal. The other four, equally spaced in the chip, store a reference level. During the readout operation, an off-chip amplifier subtracts the closest reference channel from each signal channel. This pseudo-differential mode reduces the common mode noise significantly in simultaneous read and write operation. The performance of the SCA, as measured on a dedicated test bench working in a simultaneous 40 MHz write/read operation, is summarized in Table 2. The bookkeeping of the SCA cells available for writing is done by two SCA controllers[7], one for each 64 channels.

The analog pipelines are followed by a 12 bit 5 MHz ADC (AD9220[8]) which digitizes the output of two SCAs after a level 1 trigger. The choice of which signal (gain) is to be digitized is either done automatically by the hardware (free gain) or the digitization of one, two or three gains can be programmed. For the free gain mode, the gain selector FPGA[9] compares a predefined sample (programmed as parameter) in medium gain after digitization to two thresholds. If the signal is less than the first threshold, the high gain is chosen. If the signal is greater than the second one, the low gain is chosen. The predefined sample is digitized once more in the chosen gain and the other samples (programmable up to 31) are also read. For five samples, a group of eight channels is thus read in approximately 10 μs. Event output data is formatted and sent in 32-bit words at 40 MHz (1.28 Gbit/s) to the miniROD (Read Out Device) board, which serves as readout buffer with one FIFO per group of eight channels.

In total, 38 FEBs were produced and tested. The noise measurement is shown in Table 3. The fixed sequence noise, i.e. the dispersion of the pedestals of the 144 cells of the SCA, was measured to be less than 0.2 mV. The dispersion of the electronic gains on a FEB is determined to be about 2%. The ratio of the medium to high gain is measured to be 9.2 and the ratio of low to medium gain to be 10. It was observed that on average in high gain the time of the signal peak is 1.4 ns after the medium gain signal, whereas the time of the peak of the low gain is about 0.6 ns after the high gain peak. This effect has been traced to the shaper and is corrected in the final version.

4.2 Calibration Boards

The calibration board must provide fast signals resembling closely the ionisation signal, it must be linear over a large dynamic range (at least 16 bit precision and up to the equivalent of 3 TeV of deposited energy in one calorimeter cell), and it must be uniform (< 0.25 % including signal distribution). As the readout is current sensitive, the traditional charge calibration through a capacitor cannot be used. Since

[6] austriamicrosystems AG, A-8141 Schloß Premstätten, Austria.
[7] Xilinx XC4036XL.
[8] Analog Devices, 1 Technology Way, Norwood, MA 02062, USA.
[9] ALTERA FLEX EPF6016TC144-2.

the parallel noise decreases for fast shaping, a current calibration with 0.1% precision calibration resistors has been chosen.

As shown in Figure 6, a precise DC current I_p is generated and flows into an inductor. When a pulse command is applied on the transistor Q_2, the transistor Q_1 is cut off and the current is diverted to ground. The magnetic energy stored in the inductor produces a fast voltage pulse with an exponential decay across the cable impedance and a 50 Ω termination resistor in parallel. This pulse is propagated inside the cryostat through a 7 m long 50 Ω cable and is applied across a precise injection resistor R_{inj} (0.1%) in the cold on the motherboards, close to the electrodes. One calibration channel is distributed to 8 readout channels in the middle or back sections and 32 in the strip section. Care has been taken so that adjacent readout channels are not connected to the same calibration channel in order to allow for crosstalk studies.

Ten boards were produced [25], each containing 64 channels aligned in a single row on each side of the board. The current is generated from a 18 bit DAC voltage through a voltage to current converter built around a low offset (<16 μV = 1 LSB) opamp and a JFET output transistor. The switch is made of a parallel fast transistor to obtain sub-nanosecond rise time. Surface mounted components have been used, leading to a high density of 9000 components per board. Only five precision resistors (0.1 %) per channel determine the pulse accuracy. The digital part is integrated in 13 FPGAs, including a delay chip with a step size of 1 ns. At the beginning of a run all sequences (number of DAC settings and their values, delay, the calibration channels enabled and the number of triggers) are loaded through the SPAC link.

The boards have been characterized on a test-bench. The output signal shows an exponential decay with a rise time of about 1 ns. At small amplitude the waveform starts to deviate from the pure exponential pulse. A small fast impulse is observed on top of the signal, usually referred to as "parasitic injected charge". After shaping (on the FEB), the parasitic injected charge is almost a derivative of the normal signal with an amplitude corresponding to 1.2 GeV. However, at the peak of the signal, the amplitude corresponds to 100 MeV but the effect is non linear. The integral non linearity is measured to be within ± 0.1% for the low and medium gains of the shaper, slightly worse for the high gain, due to the parasitic injected charge.

The pulse uniformity has been measured after shaping and shows a raw dispersion of 0.2 %. Apart from the contribution of the precision resistors, the main contribution comes from the different strip-line lengths from the output of each channel and the output connector. After correcting for this effect, the pulse uniformity has a rms of 0.11 %. To preserve the pulse uniformity of the board, the cable which brings the signal on the mother board has 50 Ω termination at both ends, thus guaranteeing a small sensitivity of the amplitude to the exact value of the cable characteristic impedance. The uniformity response of 64 channels has been measured at warm including a 50 Ω 64 channel harness. The characteristic impedance within the harness varied by ±5 %. No degradation is observed and a rms of 0.13 % is measured, which includes the board and the cable distribution non-uniformity (impedance and skin effect).

5 Experimental Setup

The beam tests of the barrel module-0 were carried out on CERN's H8 beam line. Electron or positron beams, as secondary and tertiary beams, with energies ranging from 10 to 245 GeV were used.

5.1 Cryostat, Cryogenics and Feedthroughs

To perform the beam test of the barrel modules, a dedicated cryostat has been built with two 4 cm thick aluminum walls separated by a 5 cm vacuum gap. The geometry of the front face of the cryostat insures that the material traversed by particles entering the cryostat is independent of the ϕ position. An argon excluder (Rohacell) located between the cold wall and the calorimeter front face reduces the amount of dead material in front of the calorimeter.

The cryostat is connected to a cryogenic system [6] common to the three ATLAS liquid argon beam test setups. It is controlled by three cooling loops: one in the expansion vessel, situated on top of the cold vessel, a large one in the cryostat, above the module, and one in the back of the module to be used also in ATLAS. The main exchanger for cool-down is the larger one above the module.

After filling, the top cooling loop (in the expansion vessel) is used to reach the required temperature-pressure point on the vapor curve. The expansion vessel is separated from the main tank by a long funnel that acts as a pressure buffer. The liquid temperature can therefore be regulated independently in the cryostat (subcooling). Liquid nitrogen is injected into the module exchanger under overpressure. The input flow is adjusted depending on the desired temperature of the liquid, while the output valve regulates the nitrogen pressure.

The temperature is stable to better than 10 mK as shown in Figure 7. The set point can be modified down to 88 K. Temperature stability is reached after about 12 hours due to the liquid and module thermal

inertia. Varying the temperature over a range of 2 K, the effect on the calorimeter response was determined to be -2%/K as shown in Figure 7.

Two feedthroughs are necessary to read the module and the two presampler sectors. FT-1 covers $0 < \phi < 0.2$ and FT0 covers $0.2 < \phi < 0.4$. Only FT0 has gold-plated pin carriers. The HV warm feedthrough is mounted above the cryostat, on the expansion vessel.

5.2 Beam Line Setup

The beam line is equipped with three scintillators in front of the calorimeter for triggering purposes (see Figure 8). The size of the last two (4x4 cm^2) defines the beam acceptance. The analog signal of S3 is read out, allowing an offline rejection of events having more than one charged track. As the trigger is asynchronous with respect to the 40 MHz clock, the time between a trigger and the next clock cycle is measured with a TDC (1 count $\sim$50 ps). Behind the cryostat, two other scintillators are used for pion and muon rejection. They can be used as veto in the trigger or in the offline analysis. The beam line is also instrumented with four multi-wire proportional chambers [26]. The first two are read via threshold discriminators, whereas the others are read via constant fraction discriminators.

The cryostat is mounted on a remote controlled table, that allows movements in η and ϕ while ensuring nominal incident angles as in ATLAS in all positions.

The air and counters in front of the cryostat correspond to 0.13 X_0. Additional material in the beam line equipment was discovered after the beam tests [27], corresponding to 0.3-0.4 X_0 distributed non-uniformly. The two aluminum walls of the cryostat, the argon excluder and the liquid argon in front of the presampler amount to 1.3 X_0 (at $\eta = 0$). The material between the presampler and the calorimeter module (cold cables and mother boards) is, non-uniform in ϕ, varying between 0.05 and 0.2 X_0 [28].

5.3 Data Acquisition and Online Monitoring

The Data Acquisition System used in the beam test setup is based on the system developed by RD13 [29]. The miniROD's FIFOs (see Section 4) are read by a RIO8061(2)[10] processor. Event building is performed by a RAID[10]. The data are compressed, written to disk and transfered automatically to the CERN central storage system (HPSS).

In all runs 7 samples of the signal (see Section 4) are recorded. Pedestal runs are taken every 8 hours with typically 2000 events. In ramp runs the DAC setting of the calibration board is increased linearly. For each pattern and DAC value, 100 events are recorded. One run is recorded in high gain and one in medium gain with DAC values covering the dynamic range of each gain. In delay runs, the DAC value is fixed, but the delay of the calibration board is increased in steps of 1 ns, thus enabling the reconstruction of the signal forms with interleaved events. For pedestal and calibration runs, 500 events are recorded, between particle bursts, for each burst.

In physics runs, about 700 events per burst are written to disk. Typically 20,000 events are recorded in each run, of which about 10% are triggered randomly. The physics runs for uniformity studies were taken in free and in fixed gain modes. The runs for the energy scan were taken only in fixed gain mode.

The data quality is assured with a monitoring program. The reconstruction is performed with the same program packages as the offline analysis. In pedestal runs the noise and pedestal values are calculated and written to the offline database. In ramp runs, the gains are calculated and written directly to the database and available for immediate use. In physics events the energy is reconstructed with a parabola, using three samples centered on the highest one, to correct for the amplitude variation due to the asynchronous trigger. The precision is sufficient to observe effects down to the percent level.

6 Electrical Modeling of the Detector

In order to calibrate and reconstruct with high precision the signal in the calorimeter, it is necessary to model the detector response and verify the accuracy of the description. Theoretical calculations have been performed and a mockup has been built.

The ionisation signal is a triangular-shaped current with a negligible rise time, decaying to zero at the end of the electron drift time ($\sim$450 ns). Electrically, the detector is traditionally modeled as a pure capacitance (C_d) of the signal electrode facing the grounded absorber with the liquid argon gap acting as dielectric ($\varepsilon_r = 1.53$). This approximation is valid below 100 MHz. The conductor for the middle section is brought past the conductor for the back section via a thin line, whose characteristic impedance can be well approximated by a series inductance (L_d). As can be seen from Figure 9, the inductance lies between the injection point for the calibration pulse and the capacitor representing the electrode. Thus when calculating the transformation between the calibration and ionization waveforms, a correction for the different injection point is necessary.

[10] CES, 38 avenue Eugène-Lance, PO Box 584, CH-1212 Grand-Lancy 1.

The capacitance of one cell is made of a capacitance C_d to the grounded absorber, proportional to the cell area, $C_d = \varepsilon_r l(17.7 + 8.39W/d)$ pF/m (l cell length, W cell width and d gap thickness in m) and the capacitance C_x to the neighboring cells, proportional to the length l and the distance to the neighbors for the middle cell : $C_x = 10.86 l \varepsilon_r$ pF/m. The capacitance of the connecting line must also be added to C_d. The inductance L for the middle cell is calculated by using the capacitance formulae $C_t = C_d + 2C_x$ and from the propagation velocity from $L = (lc)^2/(\varepsilon_r C_t)$.

In addition to the detector inductance, sizeable only for the middle section, the summing boards and motherboards described above add a significant contribution of 12 nH and a capacitance of 77 pF.

In Figure 10 the capacitances and inductances calculated are shown, as well as several measurements for the middle section. The results were obtained from a fit of the impedance response as function of the frequency from an RLC-meter. The capacitance behavior as a function of η is in fair agreement with expectations while the inductance measurements show a large increase every 8 channels. This problem has been traced back to an improper grounding : every two electrode connectors (which bring out 4 middle and 2 back channels), one ground spring was omitted in the design on one side of the connector which induces additional inductance and mutual coupling to neighbours.

In order to investigate the potential bias introduced by the inductance in the calibration of the calorimeter, a detector mock-up consisting of a sandwich of 5 absorbers and 4 electrodes has been built [30], using in the gap perforated polypropylene, whose dielectric constant is close to the one of liquid argon. The input signal is injected either on the summing board for the calibration pulse or directly on the electrode to mimic the physics pulse coming from an electromagnetic shower. Figure 11 shows the calibration and physics signal for a same input : not only the amplitude differs but the calibration pulse is distorted. The calibration amplitude corrects to first order the detector capacitance variation but not the inductance, which results in a few $^0/_{00}$/nH bias as illustrated in Figure 11. The missing ground increases the non-uniformity by about 1.5 %.

7 Signal Reconstruction

In order to compute the amplitude and time of the physics pulses taken in an asynchronous mode, a linear weighted sum of the sample ADC counts S_i, after pedestal subtraction, is used (digital filtering method):

$$A_{max} = \sum_{i=1}^{n} a_i S_i \qquad A_{max}\Delta t = \sum_{i=1}^{n} b_i S_i \tag{1}$$

where A_{max} and Δt are the pulse amplitude and the pulse peak time deviation from the assumed time. Only the five central samples are used.

To compute the optimal filtering coefficients a_i and b_i, the noise autocorrelation, the pulse shape and its derivative are required [31]. The main difficulty lies in the prediction of the physics pulse shape, taking into account the bias from the inductance described in Section 6. A full analytical description of the electrical chain has shown to have too many parameters, especially for the cable modelling (skin effect, reflections). The approach chosen takes into account that most parts of the signal readout are common to the calibration and physics pulse [32].

The energy in one cell is obtained by applying the electronic gain to the reconstructed amplitude in ADC counts, including a non-linear behavior.

7.1 Physics Signal Reconstruction

As illustrated in Figure 9 the difference between the physics and calibration pulses is due to the different input signal and the different injection point of the signals. In this approach the calibration cable is assumed to have a constant attenuation factor and the reflections are neglected. Expressing the response to a physics pulse in Fourier space, it can be shown that :

$$\mathcal{F}[U_{phy}](\omega) = \frac{\mathcal{F}[I_{phy}](\omega)}{\mathcal{F}[I_{cal}](\omega)} \frac{\omega_d^2}{\omega_d^2 - \omega^2} \mathcal{F}[U_{cal}](\omega) \tag{2}$$

where the first term takes into account the different input current, the second the different injection point, and the last one is the Fourier transform of the calibration signal which can be extracted from the calibration data. In this model the physics signal depends only on three parameters: $\omega_d = 1/\sqrt{C_d L_d}$, the starting times of the calibration and physics pulses.

Using delay runs, and subtracting the parasitic injected charge, the calibration pulse is reconstructed with a 1 ns step-size and the Fourier transform of the calibration pulse determined. The starting time of the calibration and physics signals can be deduced from the trigger system timing, cable lengths and time of flight of the particles. The detector capacitance can be calculated, but, as shown in Figure 10,

the inductance cannot be predicted. Therefore an empirical method is used. By using the phase of each event (TDC) the physics pulses in a cell can be averaged within a 1 ns bin. From a fit to this shape, the three parameters (t_0^{CAL}, t_0^{PHY}, ω_d) are extracted. In the regions where the inductance measurements were available, the agreement with the fit results is about a few nH. A typical result of this fit is shown in Figure 12 with residuals of about ± 2 %. A residual dependence of the reconstructed energy on the phase (TDC) is therefore inevitable.

For each cell, the coefficients a_i and b_i are then computed, incorporating the correction of the bias introduced by the inductance. As an example Figure 13 shows the ratio of the physics amplitude to the calibration amplitude (for a same given input) as a function of η for $\phi_{Cell} = 10$: It reflects the increase of the electrode inductance versus η and the 8 fold-pattern from the missing ground return.

7.2 Calibration of Electronics: Gain and Noise

During data taking, every 24 hours, calibration data with an increasing DAC input (typically 20 values) are recorded in each gain of the shaper. After subtraction of the parasitic injected charge, measured with DAC=0, the amplitude is reconstructed using the cell pulse shape derived from the delay run. The DAC dependence (converted to GeV) is fitted as a function of the amplitude with a second order polynomial to take into account small non linearities. The linear term is about 10 MeV/adc count in the high gain in the rapidity region $\eta < 0.8$ for the middle section. The second order term accounts to less than 1 % over the dynamic range. Over the run period the stability of the gain is better than a few parts per mil.

The noise has been studied using pedestal runs over the whole calorimeter module. The incoherent noise per channel is computed as the rms of the pedestal distribution after applying the optimal coefficients a_i. Such a reconstruction takes into account the noise autocorrelation and yields a noise reduction between 1.4 and 1.8 depending on the detector capacitance. The behavior of the noise as a function of η in each compartment is shown in Figure 14 for high gain. Except for the back layer, where the noise behavior reflects the variation of the electronics gain (detector capacitance), the noise is almost flat and well within the requirements. The coherent noise has been measured on each FEB (128 channels) and amounts to about 5 % of the incoherent contribution for each channel. For an electron cluster (see Section 9) at $\eta = 0.26$, the total noise is 143 MeV (261 MeV) in high (medium) gain, of which 95% (80%) is incoherent noise.

7.3 Free Gain Mode Performance

Since the electron energy is limited to about 245 GeV, only the lower threshold of the free gain mode can be tested with physics data. The determination of the threshold value relies on the fact that as the high gain begins to saturate, the rms (for calibration events) as a function of the DAC setting decreases for the peak sample. The average ADC value for the DAC setting where saturation starts defines the threshold. One global threshold value is determined for all FEBs.

In Figure 15 the observed ADC values of the programmed (peak) sample (see Section 4) in high and medium gain are shown. The implemented threshold is respected up to the 10^{-4} level and the threshold is sharp as expected.

No significant differences are found in the energy resolution of the fixed gain, software free gain and hardware free gain, showing that the free gain mode works well. At 245 GeV ($\eta = 0.26$) typically two (two) cells of the front (middle) layer are read in the medium gain resulting in a noise contribution to the electron reconstruction of 161 MeV.

7.4 Crosstalk

A very detailed study of the crosstalk has been performed using the delay runs taken during the various beam test periods resulting in improvements of the cold electronics. The major sources of crosstalk occuring on the electrodes themselves or through the electronic chain have been identified and quantified [33, 34, 35], providing a complete map of the crosstalk in the module 0 summarized in Figure 16.

The silk screened resistors which connect the middle and the front section on the electrodes induce a resistive crosstalk, which has the same form as the signal, between these two layers. Figure 17 (top left) shows the strong correlation between this crosstalk and the value of the resistor measured before stacking. During the two years of beam tests of the module 0 (4 cryostat cool down cycles), a follow up of the resistive crosstalk has been performed (Figure 17 (top right)) showing good stability.

The capacitive crosstalk, which has the form of a derivative of the signal, between strips cells is presented in Figure 17 (bottom left) and is in very good agreement with the calculation shown in Figure 10. Only a few channels show a larger crosstalk (10 %), identified as a short between strips in HV layers.

The crosstalk in the middle and back layer, or between these two layers shows mainly inductive contributions. The origin was traced to the summing and mother boards (which were redesigned for the last test beam period providing a reduction by a factor 1.5) and the missing spring on the electrodes. As an example Figure 17 (bottom right) shows the crosstalk of middle to back cells as a function of η: the large increase of the crosstalk every two connectors is clearly visible. The level of crosstalk, although small (less than 0.5% at signal peak, around 1-2% peak to peak), is a limitation to the reconstruction of the physics pulse shape in the back section where the crosstalk contribution from the middle layer, where most of the energy is deposited, induces a strong change of the pulse shape.

8 Response to Muons

Muons in the high energy electron beam have been used to study the EM barrel module 0 response to "minimum ionising" particles (mip). As they deposit their energy in a smaller cluster than the electrons, they can provide cleaner or complementary information on the calorimeter [36].

Since the accordion geometry induces a sharing of the energy deposition between two contiguous cells in ϕ even in the case of minimum ionising particles, the muon signal is reconstructed by using a 1×2 cluster in $\eta \times \phi$ in the middle sampling. The cell selection is made event by event, using the particle impact point extrapolated from the beam chambers.

The distribution of the cluster energy is shown in Figure 18 for muons and for "random" events. The resulting signal to noise ratio, defined as the ratio between the muon most probable energy and the rms of the noise distribution, is 7.11±0.07. A $(\frac{e}{\mu})$ ratio of 0.75 ± 0.03 can be deduced from the determination of the absolute muon energy deposition, the energy scale being calibrated with electrons. For this measurement the sampling fraction was calculated to be about 0.25 and $(dE/dx)_\mu \cdot L_{argon}$, i.e. the energy loss of muons times effective length traversed in the liquid argon, was taken from simulation. Unlike electrons, muons provide also a means to test the crosstalk measurements done with calibration runs. A qualitative agreement is observed.

The energy deposited by muons in a cell of the middle layer is shown as a function of ϕ in Figure 19, folded onto one physical gap to increase the statistic sensitivity. Two clear modulations are observed with peaks located at the absorber fold position or the electrode fold position. The peak to peak amplitude of the modulation is about 6%, which is 4 times larger than with electrons. The Monte Carlo (Geant3) simulation shows that the contribution of the variable sampling fraction due to the accordion geometry crossed as a function of ϕ by the muons predicts a much smaller effect. A simulation of the charge collection with a detailed map of the electrical field is in reasonable agreement with the data. A parallel beam was simulated (as in the data) and a smearing of the muon position corresponding to the beam chamber resolution (~ 0.4 mm) was applied. For the drift velocity, $v_D \sim E^\alpha$, $\alpha = 0.35$ was used.

Muons have also been used to study the uniformity of the module in η. Since a muon veto was applied at the trigger level during most of the data taking period, the statistics was quite poor and combinations of runs are mandatory to increase statistics. As the main possible contribution to the non-uniformity shows a eight fold effect, a folding has been applied in order to further increase the statistics. The results obtained with optimal filtering coefficients or using only the energy reconstructed with the highest sample are shown in Figure 19. With the optimal filtering coefficients the module response is uniform within the error bars of 0.4%.

9 Response to Electrons

Electron samples are selected by demanding a minimum amount of reconstructed energy in the calorimeter. In order to remove particles which have interacted upstream of the calorimeter, pions or off-momentum particles in the beam, a series of quality cuts based on the information from the beam chambers and the scintillator counters is applied. For instance, electrons producing a signal incompatible with that of a mip in the upstream scintillator S_3 are rejected.

9.1 Electron Energy Reconstruction

The electron energy is reconstructed by summing the calibrated energies deposited in the presampler and in the three calorimeter compartments. In the middle compartment, the energies of 3×3 cells, centered around the cell with the largest energy deposit, are summed. The cluster size is expressed in number of cells in $\eta \times \phi$. In the back compartment 2×3, in the front section 24×1 cells and in the presampler 3×1 cells are summed to cover at least the same area as in the middle section. In the front section and the presampler the cluster size in ϕ is doubled if the ϕ-boundary of the central cell of the middle coincides with a boundary of a front (or presampler) cell. The cluster is similar to the one foreseen for ATLAS [37]. The electron energy contained in the cluster is about 90% of the total electron energy. In each compartment, the cluster position is calculated as the energy weighted barycentre.

The typical energy sharing among different compartments, as a function of η, is shown in Figure 20, for two incident energies $E_{\rm beam}$ = 245 GeV and 20 GeV. The energy fraction deposited in each layer depends on the beam energy and reflects the energy dependence of the longitudinal shower profile and the variation of the longitudinal segmentation as function of η.

To correct for the energy loss upstream of the calorimeter, mainly due to the cryostat walls, the energy deposited in the presampler is weighted by a factor $\alpha > 1$. Longitudinal energy leakage induces a deterioration of the energy resolution, therefore a weight (β) is also applied to the energy deposited in the back compartment:

$$E = \alpha E_{ps} + E_{front} + E_{middle} + \beta E_{back} \tag{3}$$

α and β are obtained by minimizing the energy resolution for each η position [38]. A typical example of the weight optimization at 245 GeV is presented in Figure 21. The weight on the back compartment as function of η varies from 1.5 to 2.5. Additionally, for incident electron energies less than 40 GeV, the energy of the back compartment is not added to the cluster, because it is dominated by electronic noise and crosstalk from the middle compartment.

As mentioned in Section 5, the temperature dependence of the reconstructed energy has been measured and is corrected. Due to the limited energy containment of the cluster, the energy depends on the impact point within a cell as shown in Figure 22. In η, this dependence is corrected with a second order polynomial. In ϕ, the effect is convoluted with the non-uniformity of the local sampling fraction and electrical field due to the accordion geometry. The correction consists of two sinusoidal functions multiplied by a second order polynomial. The peak to peak amplitude before correction is less than 2%. This is about four times less than for muons because of the lateral spread of the shower energy for electrons. After correction the residual rms is about 0.2%.

After signal reconstruction a residual dependence of the amplitude with respect to the phase between the trigger and the 40 MHz clock is observed and corrected.

9.2 Energy Resolution

The energy is reconstructed in fixed-gain mode: high (medium) gain for energies less (greater) than 60 GeV. Figure 23 shows the energy spectra reconstructed in the calorimeter for electrons of energies 10 and 245 GeV. The absolute energy scale computed from first principles (energy deposited in the liquid, sampling fraction, response of the electronics chain) is correct at the level of 5%. In spite of the quality cuts applied, low energy tails are observed. These events are attributed to interactions in the upstream material, which is distributed non-uniformly in the beam line, and a residual pion contamination [27]. In order to reduce the sensitivity of the calorimeter resolution to these tails, the spectrum is fit with a Gaussian starting at -2σ off the mean value.

The energy resolution measured at three rapidity points is presented in Figure 24 in the A electrodes ($\eta < 0.8$) only, as a complete energy scan is not available in the B electrodes. The noise term extracted from random triggers, in agreement with the noise obtained from Pedestal runs, and the beam energy spread [39] have been subtracted at each energy. The resulting experimental points have been fit with the expression :

$$\frac{\sigma_E}{E} = \frac{a}{\sqrt{E}} \oplus b \tag{4}$$

where a is the stochastic term, b the constant term reflecting local non-uniformities in the calorimeter response, and E the energy expressed in GeV. Sampling and constant terms are summarized in Table 4, where the errors are statistical only. A variation of the energy range included in the fit would result in variations on the sampling and constant terms by at most 0.5% and 0.1% respectively. The stochastic terms as well as the sampling terms are within expectation with the exception of the local constant term at $\eta_{Cell} = 3$ ($\eta = 0.0875$). There the larger constant term is attributed to the reduced depth of the calorimeter and the difficulty to correct the energy leakage.

The behavior of the sampling term of the energy resolution as a function of the pseudorapidity has been studied with the position scans of the module, recorded with incident electrons at 20 GeV, for which the sampling term contribution is dominant. The result, beam energy spread subtracted, and the Monte Carlo expectation are shown in Figure 25. The variation of the sampling term from $\eta = 0$ to $\eta = 0.8$ follows $1/\sin\theta$ law, as expected from the decrease of the sampling frequency as a function of the angle of incidence. For $\eta > 0.8$, the degradation of the sampling term in data and Monte Carlo is stronger than the pure geometrical expectation due to the impact of the material upstream of the calorimeter.

The linearity of the detector response is measured to be $\pm 1\%$ from 20 to 245 GeV. No fine study of the linearity was performed due to the amount of material in the beam-line. The calorimeter response has been also studied with increasing beam intensity to simulate pile-up conditions at LHC. A drop of

the high voltage and/or ion build up could appear. Up to intensities comparable to the energy flux from pile-up at LHC in the barrel, no shift of the mean energy larger than 4 ‰ has been observed.

The stability of the calorimeter's response as function of time was measured by using the runs ($E_{Beam} = 245$ GeV) periodically recorded at the same (reference) position. The rms of the response over a period 9 days was measured to be 240 MeV.

9.3 Response Uniformity

The uniformity of the calorimeter response as a function of the electron impact point has been studied by using position scan data collected over a large part of the detector volume (corresponding to 144 cells of the middle compartment) with a high energy (245 GeV) electron beam. A non uniform energy response, arising for instance from mechanical, geometrical, calibration, material effects, translates into a large constant term of the energy resolution. The ATLAS goal [37] is to achieve a constant term of 0.7% or smaller over the full calorimeter acceptance. The strategy to reach this goal is described in detail in [37], and requires in particular that a constant term of $\leq 0.5\%$ can be obtained over a calorimeter region of size $\Delta\eta \times \Delta\phi = 0.2 \times 0.4$ (corresponding to 128 middle cells).

In the analysis of the scan data, the electron energy was obtained as described in the previous sections. The same correction functions were applied to all cells, whereas the values of the parameters were varied by blocks of cells typically of size $\Delta\eta = 0.4$.

Figure 26 shows the reconstructed energy as a function of η as obtained in three ϕ rows (left plot). At each ϕ, 48 middle cells have been scanned, which corresponds to a rapidity region $0 < \eta < 1.2$, i.e. almost the full coverage of a half barrel calorimeter. From this sample, only three cells have been discarded at the analysis level, one because it is adjacent to a dead cell and two because they have unstable calibration gains. This gives a total of 141 cells. The various ϕ rows show a similar behavior. A small response drop is observed at position $\eta_{Cell} = 31$ ($\eta = 0.7875$)), i.e. at the transition between electrodes A and B. This region requires a dedicated calibration of the detector response, which is beyond the scope of this paper. Another drop at $\eta_{Cell} = 11$ ($\eta = 0.2875$) was attributed to the beam test setup (damaged cable) and not to the calorimeter behavior.

The response dispersion (Figure 26) is about 0.6% in each ϕ row. A similar result was obtained from a smaller size scan collected with 20 GeV electrons. This indicates that possible non-uniformities related to the particle energy (arising for instance from leakage at high energy, or the impact of material at low energy) are well cured by the applied corrections.

The constant term of the energy resolution over a large area can be obtained from the overall energy spectrum of all electrons collected in the above-mentioned 141 spots. This is shown in Figure 27. About 1 million events enter this plot. The low-energy tail is due mainly to material effects and residual pion contamination. The constant term of the energy resolution can be obtained from a Gaussian fit to this spectrum over the region not affected by the tail, after unfolding the beam momentum spread and the measured sampling and noise terms. The result is 0.78%. It should be noticed that this result can not be directly compared with the 0.5% quoted above, which is the goal over an area of $\Delta\eta \times \Delta\phi = 0.2 \times 0.4$, since it is obtained over an area of $\Delta\eta \times \Delta\phi = 1.2 \times 0.075$, i.e. much larger in η. Indeed most of the non-uniformities (e.g. due to the upstream material) are expected to show up in this projection.

10 Conclusions and Prospects

The pre-series module 0 for the future barrel electromagnetic calorimeter of ATLAS has been built and successfully tested. It has been shown that the absorbers can be built with a sufficiently small thickness spread, so that their expected contribution to the constant term is only 0.15%, i.e. well within requirements. The transition to electrodes of larger size proved to be difficult, but feasible. The absorbers, electrodes and spacers were assembled with an over-thickness of less than 0.3 mm. Two presampler sectors were built and tested successfully.

Calibration boards and front end ATLAS-like boards have been built and tested. The calorimeter module and the presampler sectors were exposed to muon and electron beams with energies of up to 245 GeV on CERN's H8 beam line, read out and calibrated with these boards, validating the module and presampler and the design of the electronics. In these beam tests the signal to noise ratio for muons has been measured to be 7.11 ± 0.07. Additionally the muon uniformity measurement as function of η showed that the signal reconstruction with optimal filtering, where the difficulty lies in the empirical correction of the inductance, is well under control. The energy resolution of calorimeter and presampler has been determined with electron beams of up to 245 GeV on the same beam line. A sampling term of less than $9.5\% \cdot \mathrm{GeV}^{1/2}/\sqrt{E}$ and a local constant term better than 0.3% have been obtained. The uniformity of the response to electrons in an area of $\Delta\eta \times \Delta\phi = 1.2 \times 0.075$ was measured to be better than 0.8%. The test beam results are in agreement with Monte Carlo simulation expectations.

The experience gained from the production of the pre-series module 0 resulted in several improvements in the production and quality control of the series modules. In the design of the electrodes, the resistors have been displaced from the bend as far as possible to decrease the number of damaged resistors. New sets of films were produced to include the missing ground connector. The typical yield in electrode production was markedly improved, being routinely above 80%. Additionally, in order to improve the geometry (folding angle) of the electrodes after bending, a new bending technique is used.

In parallel to the use of the current front end electronics in the beam tests, a crate with radiation tolerant electronics will be built and tested by the end of 2002. In 2001 and 2002 four series modules of the barrel electromagnetic calorimeter will be studied in the H8 beam line. The improvements with respect to the pre-series module 0 and their performance in terms of energy resolution, linearity and uniformity will be assessed.

Acknowledgements

We are indebted to our technicians for their contribution to the construction and running of the barrel module 0 and the electronics. We would like to thank the accelerator division for the good working conditions in the H8 beamline. Those of us from non-member states wish to thank CERN for its hospitality. We are grateful to M. Lefebvre for his careful reading of the manuscript.

References

[1] RD3 Collaboration, *Nucl. Instrum. Methods* A **309** (1991) 438.
[2] RD3 Collaboration, *Nucl. Instrum. Methods* A **321** (1992) 467.
[3] RD3 Collaboration, *Nucl. Instrum. Methods* A **325** (1993) 118.
[4] RD3 Collaboration, *Nucl. Instrum. Methods* A **364** (1995) 290.
[5] ATLAS Collaboration, *Calorimeter Performance Technical Design Report*, CERN LHCC/96-40.
[6] ATLAS Collaboration, *Liquid Argon Calorimeter Technical Design Report*, CERN LHCC/96-41.
[7] B. Mansoulié, *Non-uniformity of lead plates and gaps: Analytical estimates of the shower averaging effect*, ATL-LARG-98-099.
[8] F. Fleuret, B. Laforge, Ph. Schwemling, *Constant Term Evolution with Lead Plate Thickness Fluctuations in EM Module 0*, ATL-LARG-2000-002.
[9] F. Fleuret, B. Laforge, Ph. Schwemling, *Lead Matching and Consequences on the EM Module 0 Constant Term*, ATL-LARG-99-014.
[10] G. Garcia et al., *Nucl. Instrum. Methods* A **418** (1998) 513.
[11] P. Puzo, Ph. Schwemling, *Tridimensional measurements of the Barrel absorbers (Module 0)* ATL-LARG-2001-004.
[12] W. Bonivento, D. Lacour, *Acceptable Values of Resistances on Electrodes of the ATLAS e.m. Calorimeter*, ATL-LARG-99-019.
[13] W. Bonivento, G. Costa, M. Mazzanti, *The electrode test setup developed in Milano: experience with RD3 and ATLAS prototypes* ATL-LARG-97-070.
[14] F. Astesan et al., *Description and Performances of the Electrical Test Benches for Readout Electrodes of the ATLAS EM Calorimeter* ATL-LARG-99-005.
[15] J. Boniface et al., *Test bench of the barrel calorimeter modules* ATL-LARG-2001-007.
[16] W. Bonivento et al., *Nucl. Instrum. Methods* A **451** (2000) 492.
[17] M.L. Andrieux et al., *Nucl. Instrum. Methods* A **479** (2002) 316.
[18] J.Y. Hostachy and J. Collot, *Slanted or Straight Electrodes for the Barrel E.M. Presampler*, ATL-LARG-98-090.
[19] A. Belymam et al., *Tests of the presampler electrodes for module 0*, ATL-LARG-2000-008.
[20] R. Bernier et al., *SPAC: Serial Protocol for the Atlas Calorimeter*, ATL-LARG-98-093.
[21] R. Bernard and J.F. Renardy, *Fast Signals Distribution for Module 0*, ATL-AL-CEA-ES-4.0.
[22] Y. Jacquier, *Préamplificateur de courant bas-bruit pour le calorimètre électromagnétique d'ATLAS*, LAL-97-56.
[23] J. Collot et al., *The LAr Tri-Gain Shaper*, ATL-LARG-98-092.
[24] Y. Jacquier et al., *Strengths and Weaknesses of Digital Filtering*, ATL-LARG-97-080.
[25] J. Colas et al., *The LARG Calorimeter calibration board*, ATL-LARG-2000-006.
[26] J. Spanggaard, *Delay Wire Chambers - A Users Guide*, SL Note 98-023-BI.
[27] I. Efthymiopoulos and K. Elsener, SL-Note-2002-018.
[28] P. Perrodo, *Material between the presampler and the EMB module 0*, ATLAS-LARG-2001-002.
[29] RD13 Collaboration, *Status Report of a Scalable Data Taking System at a Testbeam for LHC*, CERN LHCC–95–47.

[30] M. Citterio et al. *A study of the electrical properties of the signal shapes in the ATLAS Liquid Argon Accordion Calorimeter using a hardware model*, ATL-LARG-2001-018.
[31] W.E. Cleland, E.G. Stern, *Nucl. Instrum. Methods* A **338** (1994) 467.
[32] L. Neukermans, P. Perrodo and R. Zitoun, *Understanding the ATLAS electromagnetic barrel pulse shapes and the absolute electronic calibration.* ATL-LARG-2001-008
[33] J. Colas et al., *Crosstalk in the ATLAS electromagnetic calorimeter* ATL-LARG-2000-04.
[34] F. Hubaut, B. Laforge, D. Lacour, F. Orsini, *Test beam Measurements of the Crosstalk in the EM Barrel Module 0*, ATL-LARG-2000-007.
[35] F. Hubaut, *Crosstalk Measurements in the EM Barrel Module 0 from 99', May 00' and July 00' Beam Tests*, ATL-LARG-2000-009.
[36] A. Camard et al., *Study of the EM barrel module 0 with muons*, ATL-LARG-2001-017.
[37] ATLAS Collaboration, *ATLAS Detector and Physics Perfomances Technical Design Report*, CERN/LHCC/99-14 (Volume I) and CERN/LHCC/99-15 (Volume II), 25 May 1999.
[38] Marco Delmastro and Marcello Fanti, *Energy resolution optimization through layers measurements weighting: analytical solutions and numerical strategies*, ATL-LARG-2002-002.
[39] *Introduction to the use of the H8 beam*, SL/EA/KE (unpublished).

Table 1: Readout segmentation of a barrel module for $\eta < 1.3$.

Compartment	$\Delta\eta$	$\Delta\phi$	X_0
Front	0.025/8	$2\pi/64$	2.5 to 4.5
Middle	0.025	$2\pi/256$	16.5 to 19
Back	0.050	$2\pi/256$	1.4 to 7

Table 2: Performance of the SCA on a test-bench.

Noise	300 μV
Dynamic range	13.3 bits
Cell to cell gain variation	<0.02%
Voltage droop rate	< 3mV/ms
Integral non linearity	< 0.1%
Cell sampling jitter	< 9 ps rms

Table 3: Average noise measured on the test-bench ($C = 0.3$ nF for 50 Ω and $C = 1$ nF for 25 Ω boards). The high gain noise is dominated by the preamplifier and the low gain noise by the ADC.

Preamplifier	High Gain	Medium Gain	Low Gain
50 Ω 1 mA	7.0 mV	1.0 mV	0.6 mV
25 Ω 5 mA	5.5 mV	0.9 mV	0.6 mV
25 Ω 10 mA	3.6 mV	0.8 mV	0.6 mV

Table 4: Sampling and constant terms obtained from fits to the data at different η.

η_{cell}	ϕ_{cell}	η	ϕ rad	a $\%\cdot\mathrm{GeV}^{1/2}$	b %
3	10	0.0875	0.2625	9.11 ± 0.12	0.47 ± 0.02
14	10	0.3625	0.2625	9.24 ± 0.10	0.23 ± 0.04
21	10	0.5375	0.2625	9.23 ± 0.09	0.21 ± 0.02

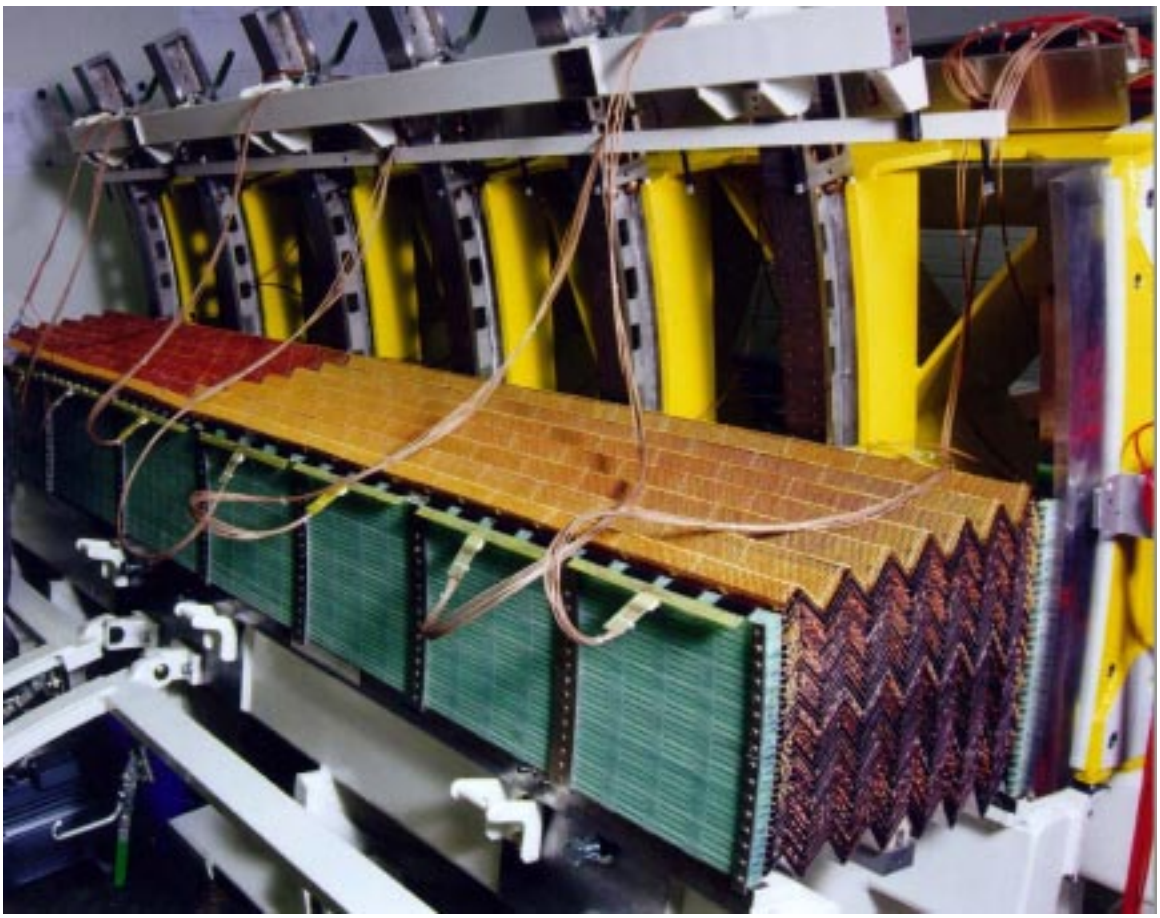

Figure 1: View of the partially stacked module 0. The position $\phi = 0$ corresponds to the 64th absorber stacked.

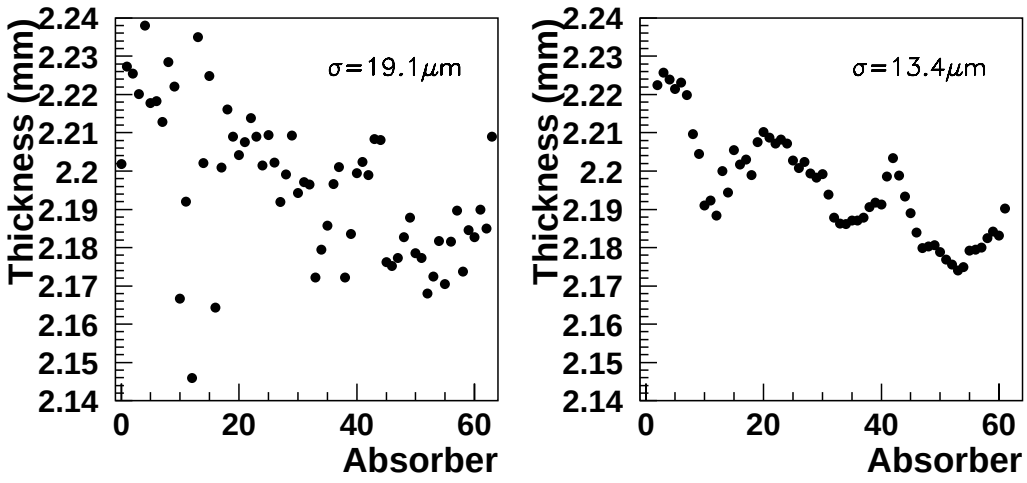

Figure 2: Absorber thickness profiles for module 0 showing raw thicknesses (left) and sliding average over 5 absorbers (right).

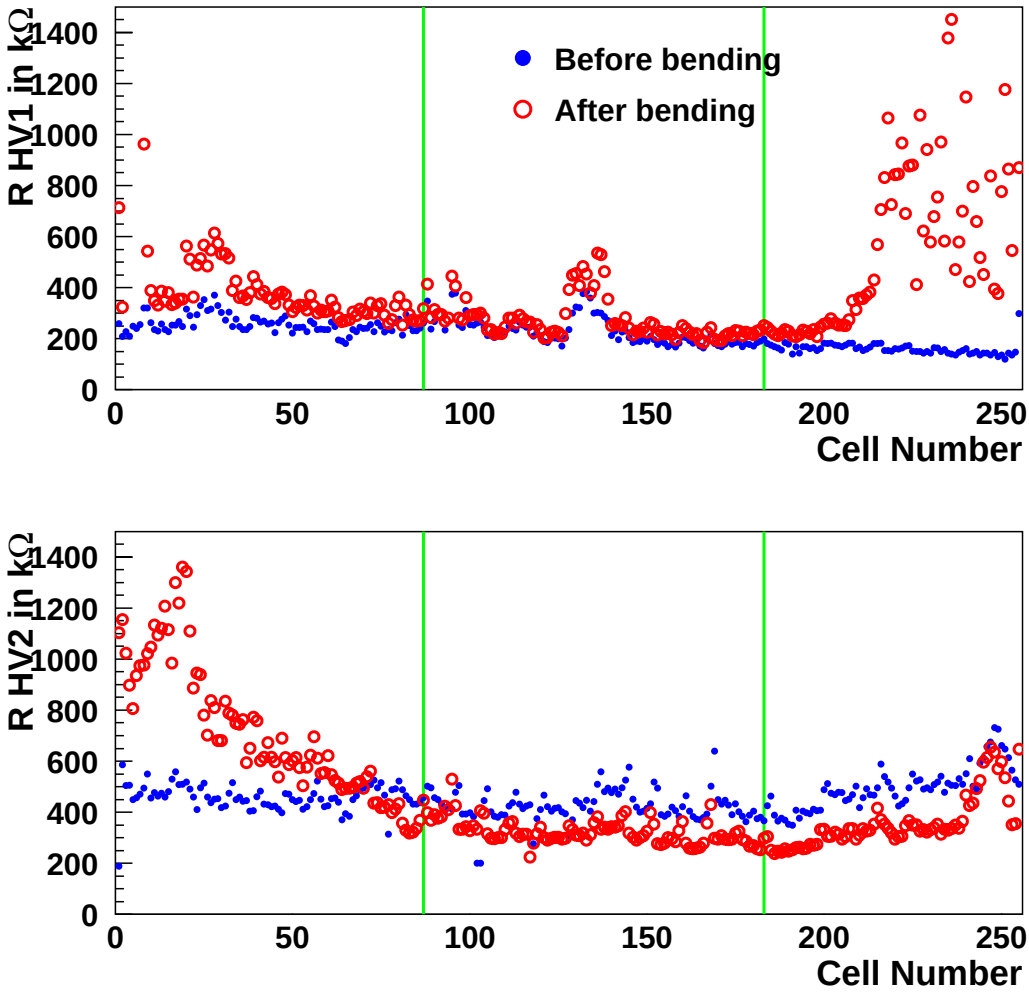

Figure 3: Front-Middle separation resistors for both sides of one electrode (type A), measured before and after bending to accordion shape as a function of the front layer cell number. Damaged resistors have larger values after bending. In the left and right section of the Figures, the resistors are within 10 mm of the bend.

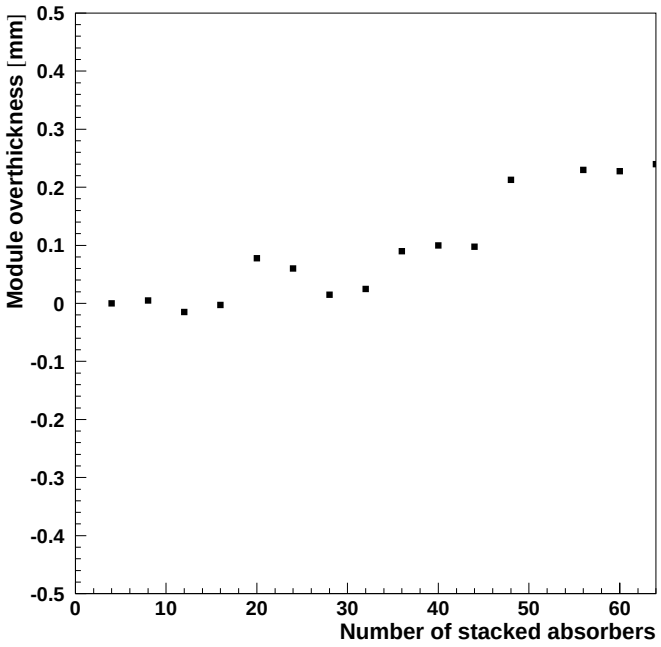

Figure 4: Module over-thickness evolution at the external radius as a function of the number of absorbers.

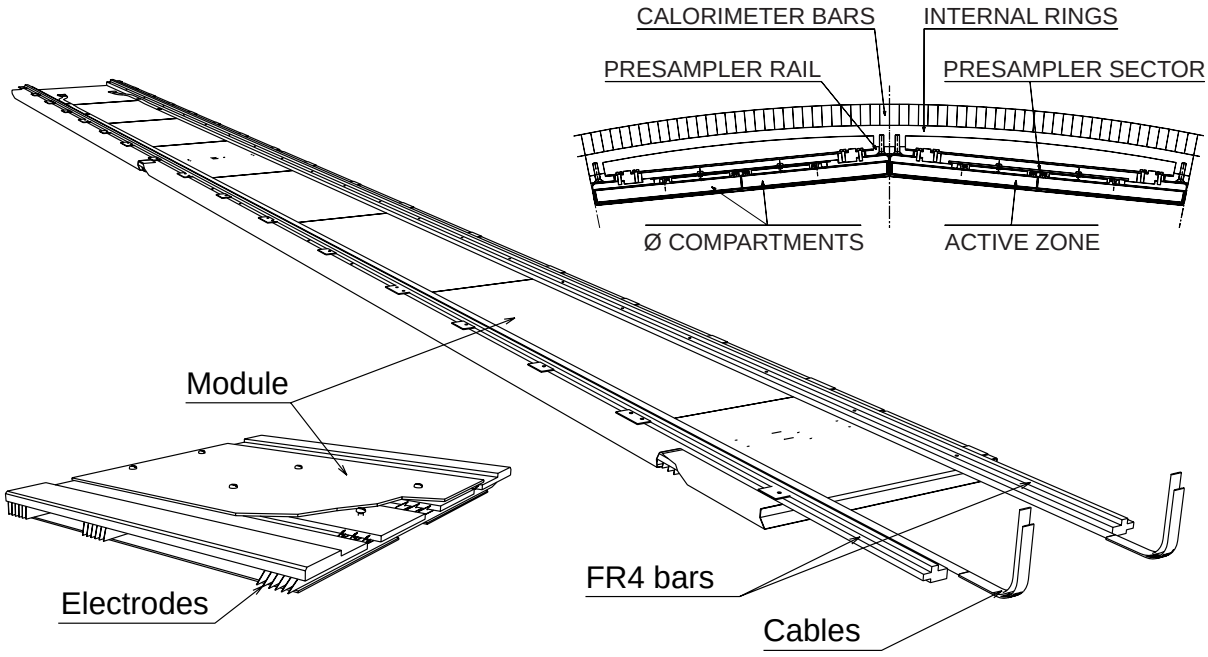

Figure 5: Perspective view of a presampler sector. Top right: calorimeter bars with two presampler sectors in front.

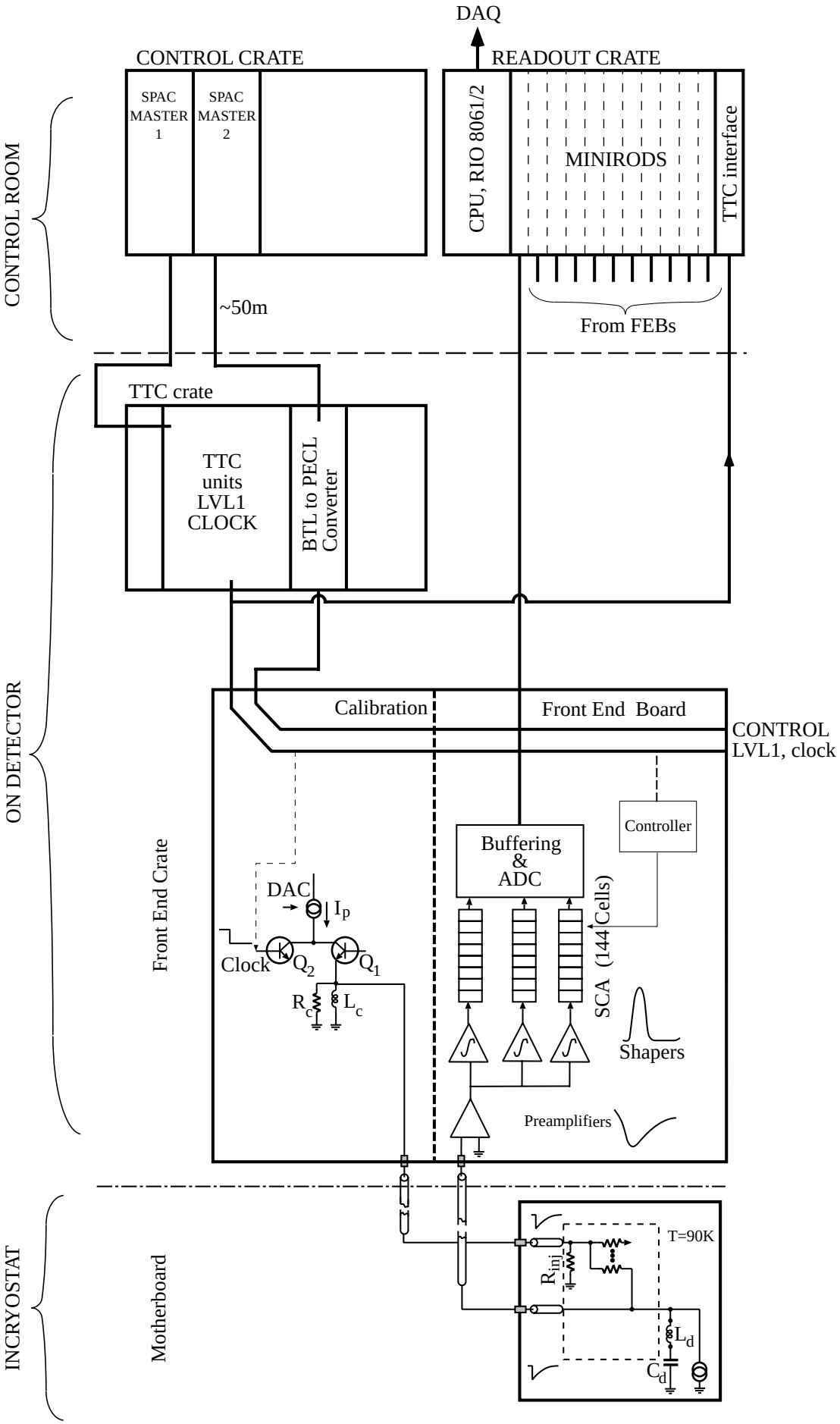

Figure 6: Schematic of the calorimeter readout.

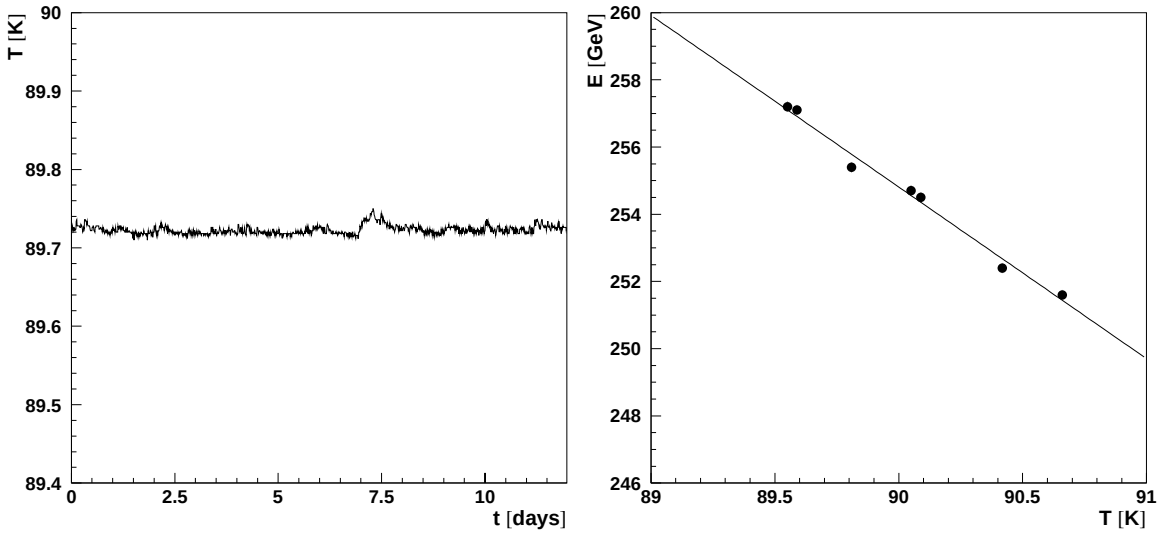

Figure 7: (Left) Liquid argon temperature variation over time for a run period. The rms is 7 mK. (Right) Energy variation as function of the liquid argon temperature measured in the middle section ($\eta_{Cell} = 14$, ϕ_{Cell}=10).

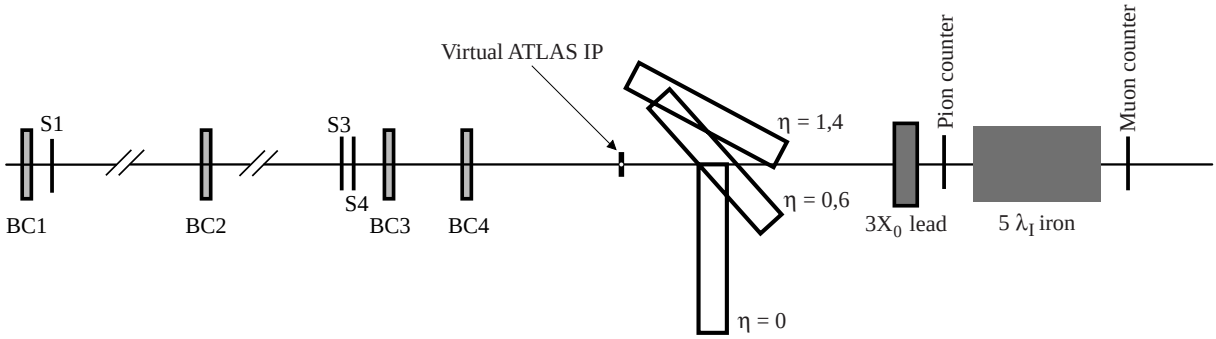

Figure 8: H8 beam line setup.

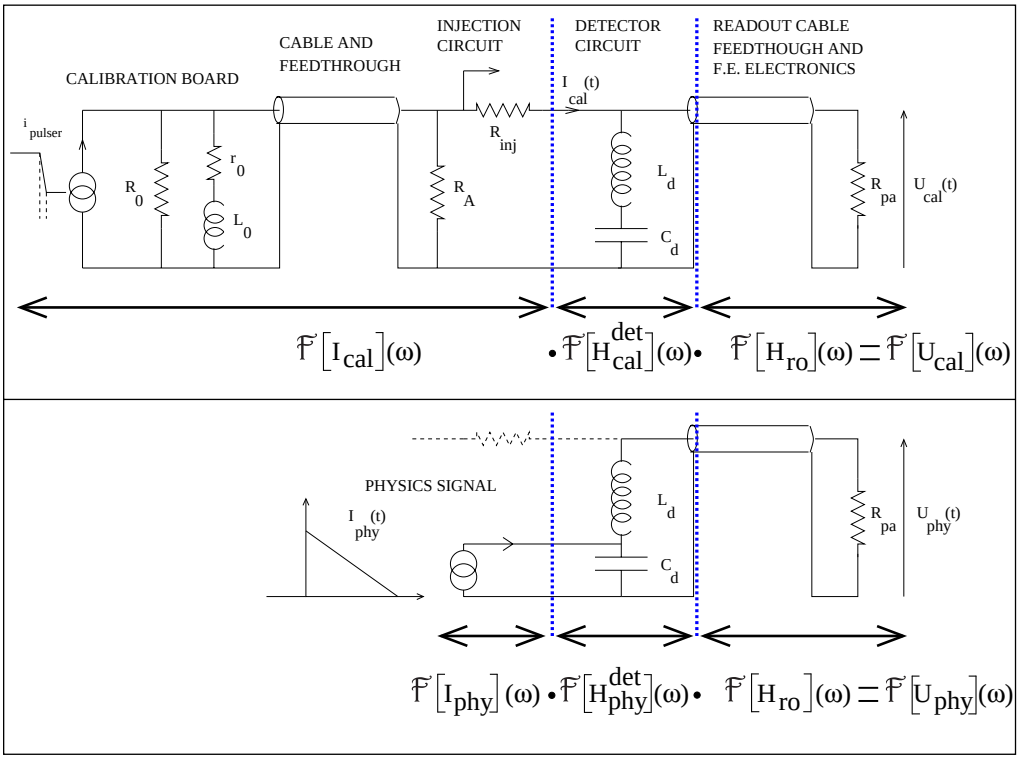

Figure 9: Electrical description of one channel of the calorimeter. The top drawing shows the calibration system and how the calibration pulse is injected into the calorimeter readout chain. The bottom drawing explains where the physics signal is injected into the same readout chain.

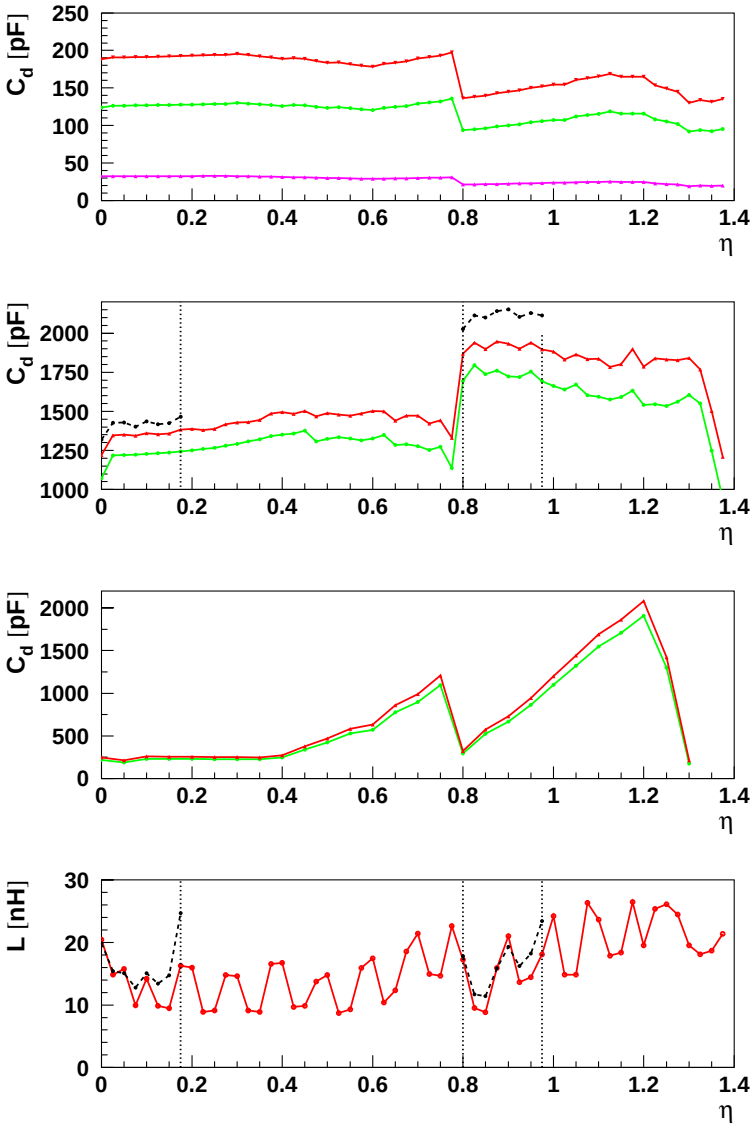

Figure 10: All plots as function of η. Top plot: total capacitance (top curve), cell capacity (middle curve) and crosstalk capacity (bottom curve) of the front section. Second plot: cell capacity (bottom curve) and total capacity (top curve) of the middle section. Third plot: cell capacity (bottom curve) and total capacity (top curve) of the back section. Bottom plot: inductance of middle cells The experimental measurements (dotted curves) contains an offset coming from the measurement system.

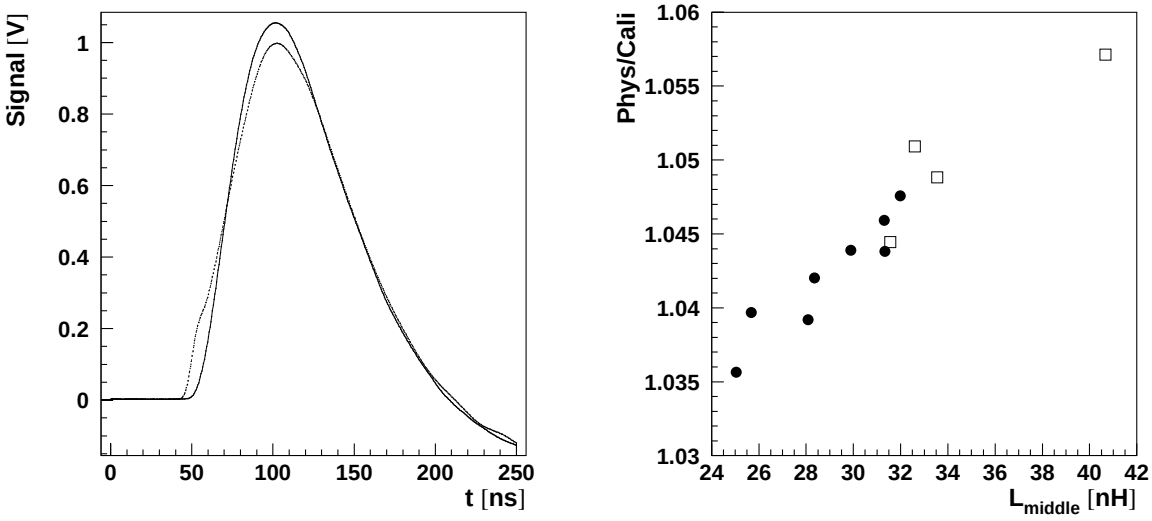

Figure 11: (Left) Typical waveforms for a physics-like (solid curve) and a calibration (dotted curve) pulse from the mock-up. (Right) Ratio of the physics-like amplitude to the calibration amplitude as function of the inductance for two ground springs (solid circles) and one ground spring (open squares), showing a clear correlation.

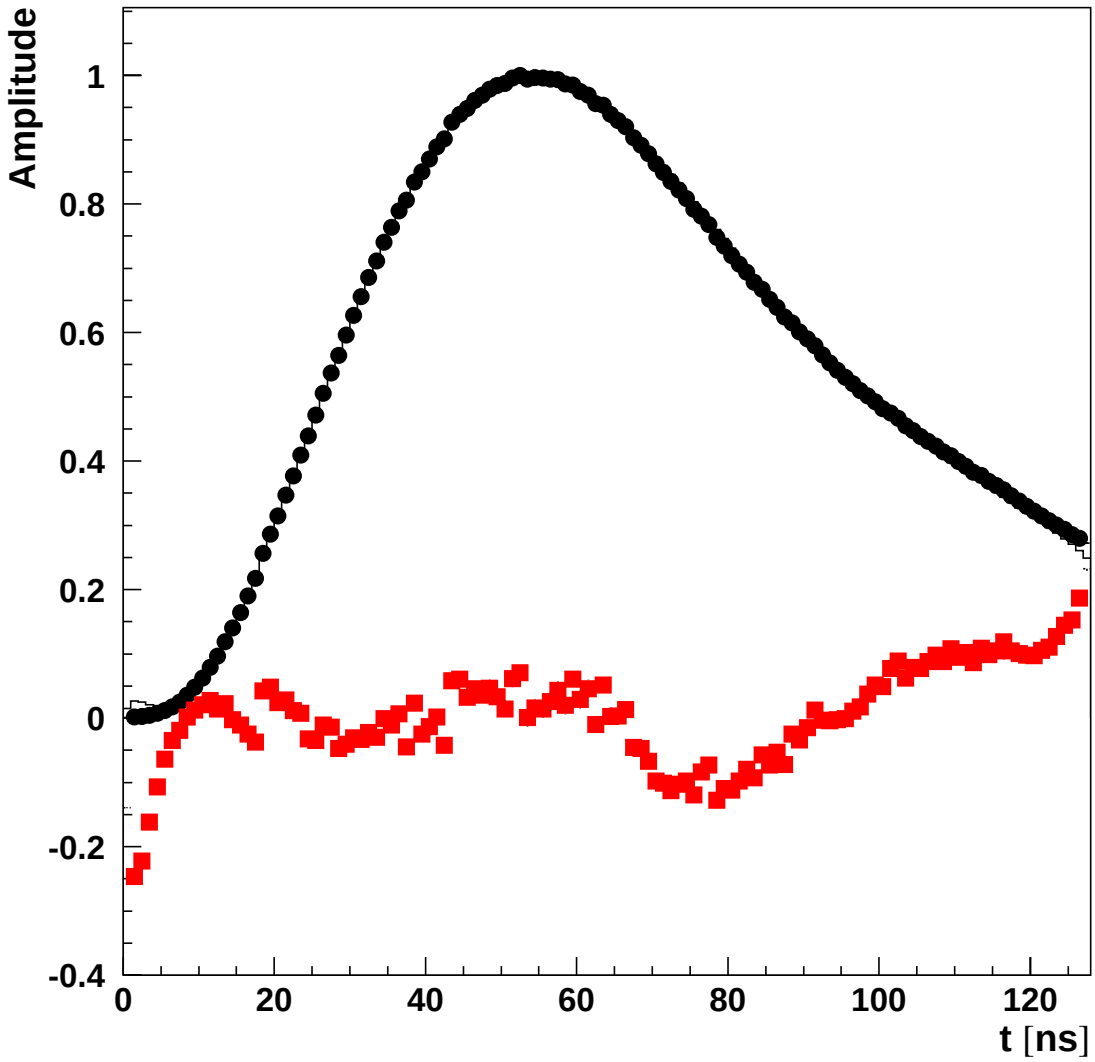

Figure 12: Data (points), fit (histogram) and residuals times 10 (squares) as a function of time for a cell of the middle section.

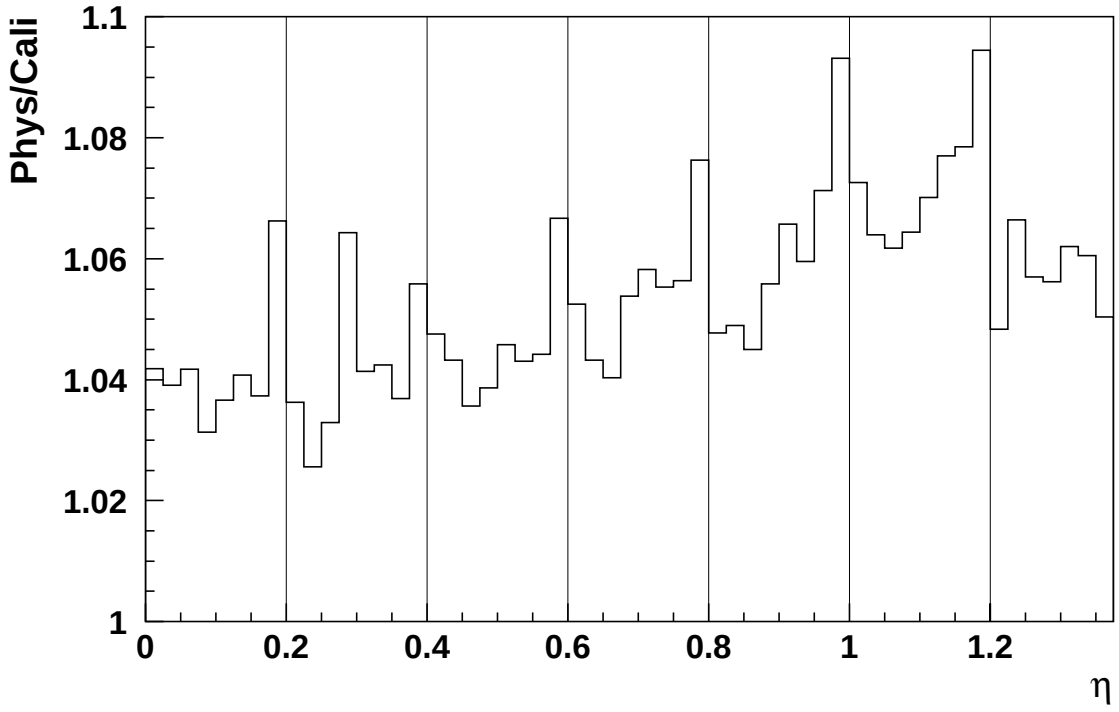

Figure 13: Predicted physics over calibration amplitude ratio versus η for middle layer cells for the line $\phi_{Cell} = 10$.

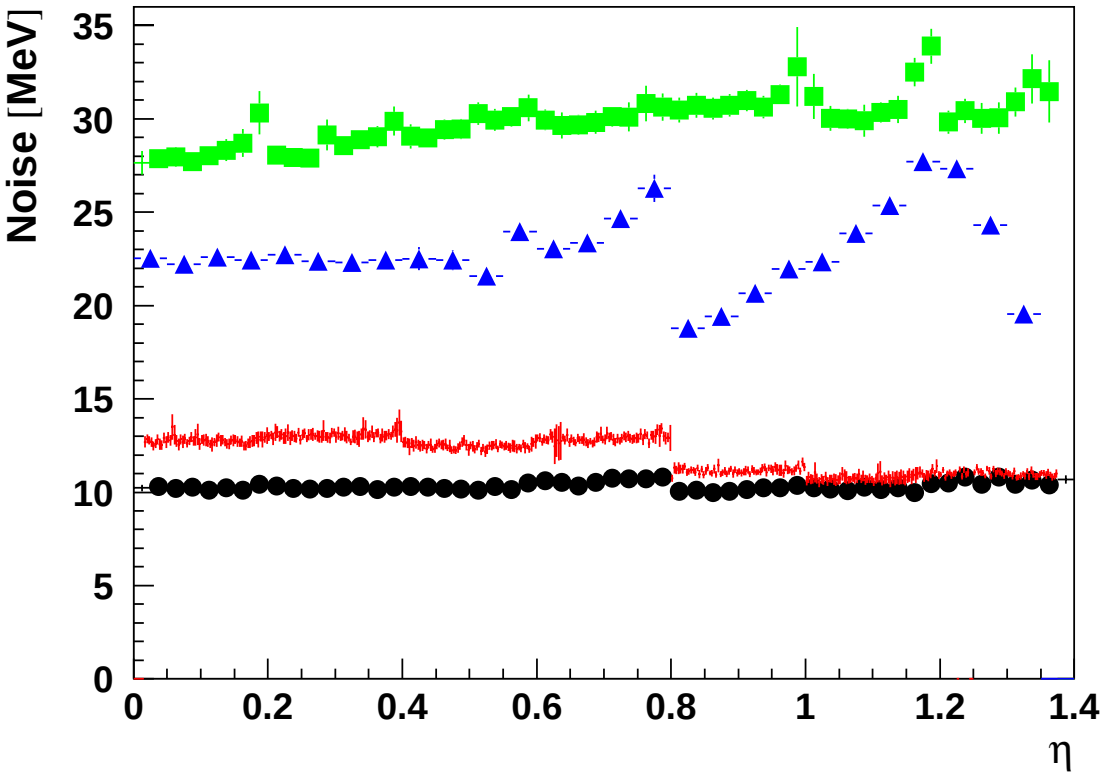

Figure 14: Noise rms, averaged in ϕ and over all pedestal runs, in high gain for the presampler (circles), front (points), middle (squares) and back (triangles) sections as a function of η.

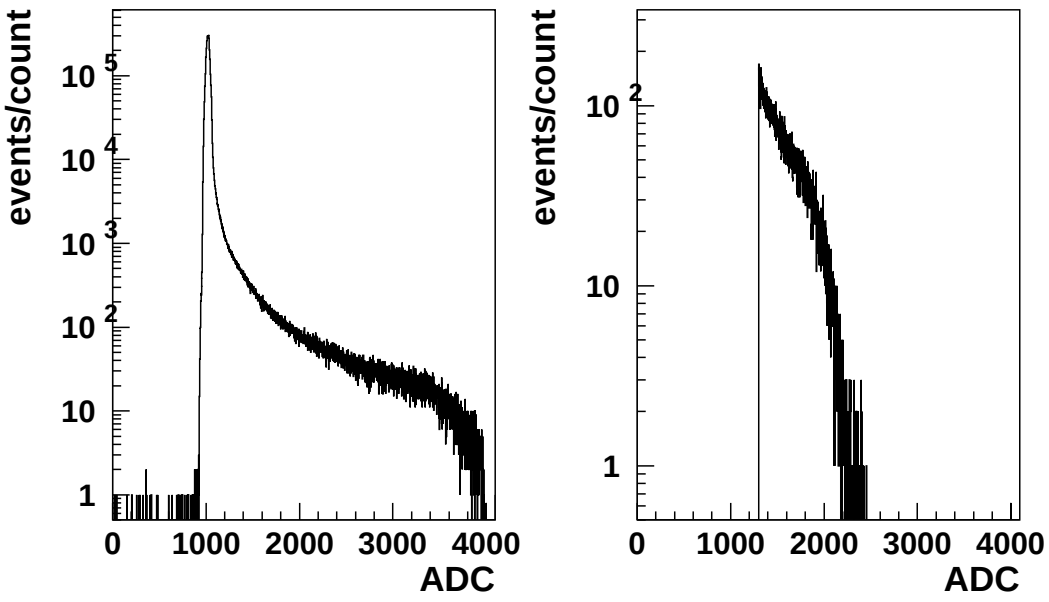

Figure 15: ADC values observed in high gain (left) and medium gain (right) of the free gain choice sample. The sharp edge at the low threshold for the medium gain shows that the algorithm works correctly. The high gain figure shows that its entire range is used.

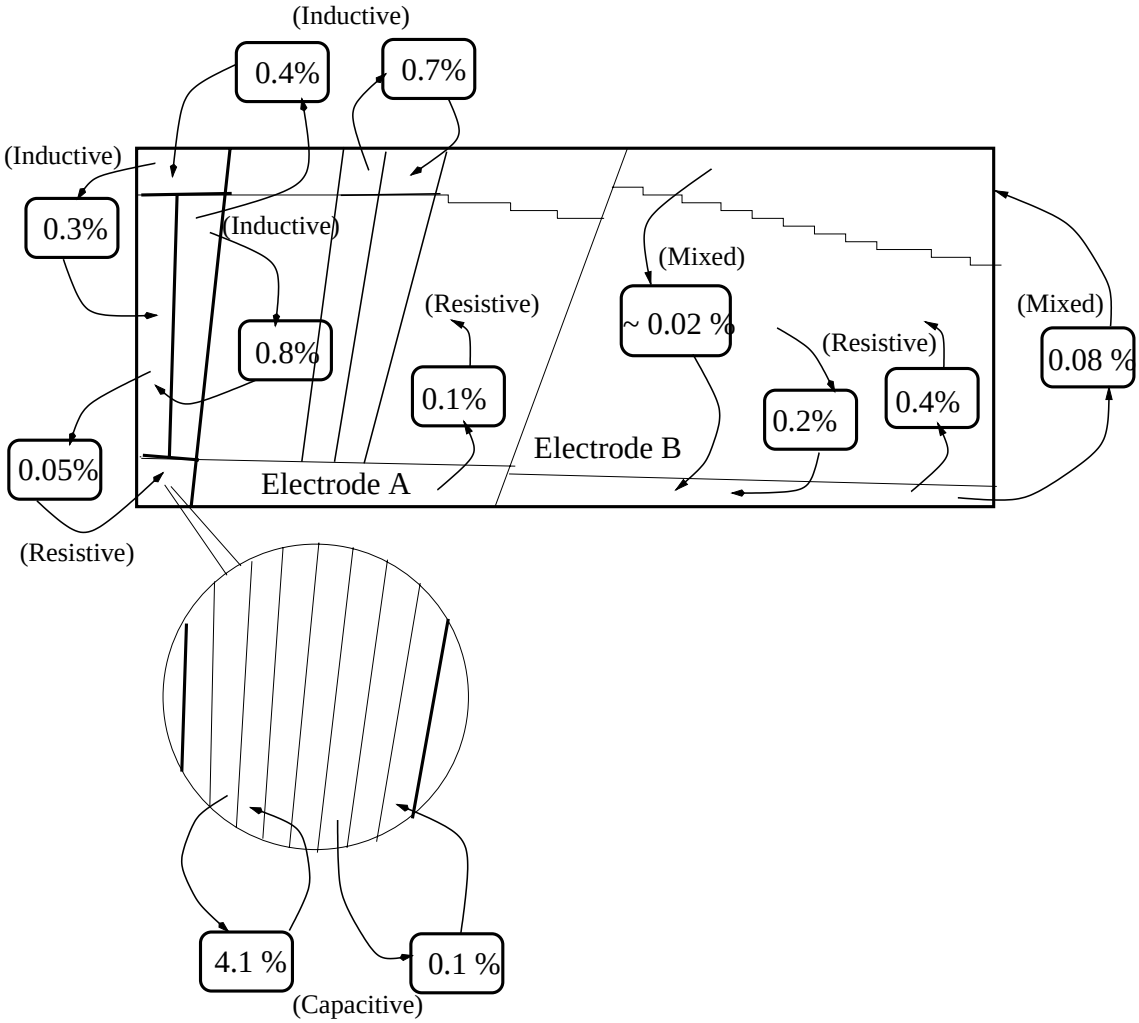

Figure 16: Summary of the crosstalk contributions in the EM barrel module 0. The crosstalk is evaluated at the peak of the pulsed signal.

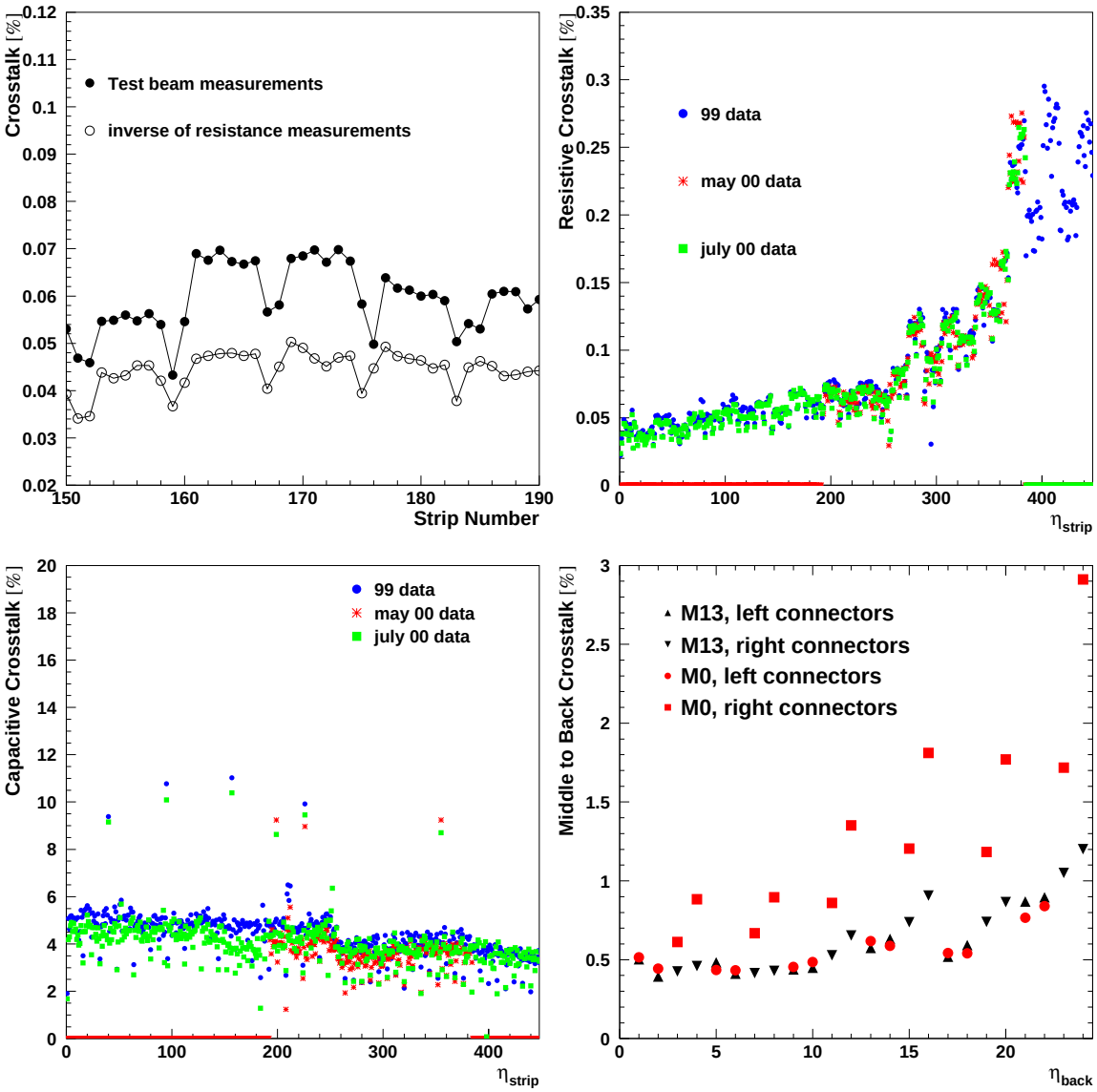

Figure 17: (Top left) Comparison of the resistive crosstalk and the inverse of the resistor (arbitrary scale) measured before stacking. (Top right) Resistive crosstalk measurements between the middle and the front sections, extracted from 1999, May and July 2000 beam tests. (Bottom left) Capacitive crosstalk measurements between one pulsed strip and its right neighbor as a function of η, extracted from 1999, May and July 2000 beam tests. (Bottom right) Inductive crosstalk of middle to back cells in module 0 (M0) (circles and squares) as a function of η. The triangles show the results on a recent production module (M13) of the ATLAS calorimeter where the missing ground return has been added.

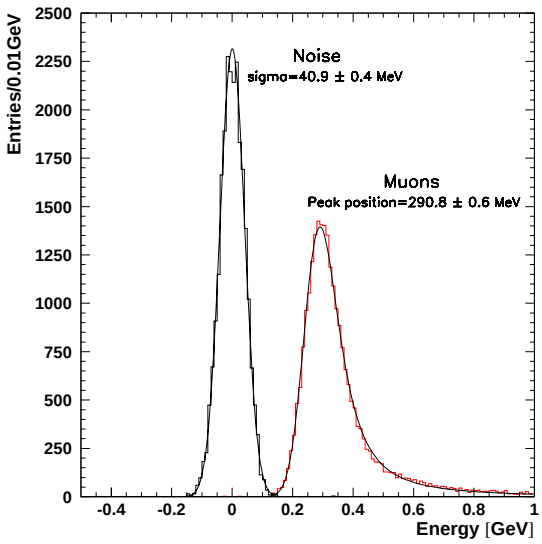

Figure 18: Muon signal produced in the calorimeter and noise distribution. The signal is fitted with a Landau distribution convoluted with a gaussian and the noise is fitted with a gaussian. The absolute energy scale is calibrated with the electrons.

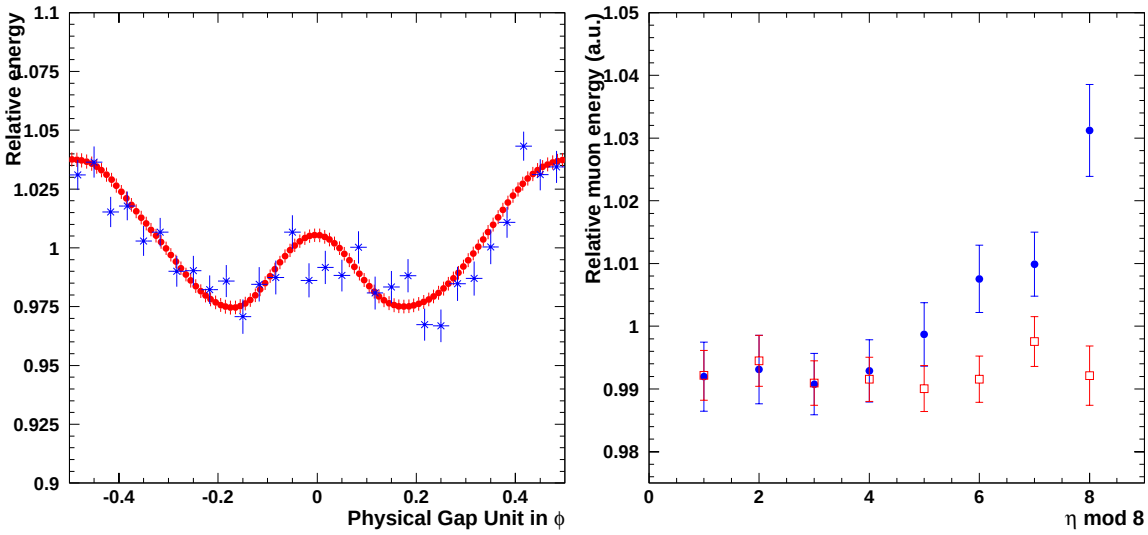

Figure 19: (Left) Modulation of the calorimeter response (normalised to 1) to muons along the ϕ direction at η_{Cell}=14 over one physical gap for simulation and data (points). (Right) Relative muon energy as a function of η, after folding of the cells with the same 8-fold η-periodicity. Error bars are at the level of 0.4%. The muon energy is reconstructed either with optimal filtering method (open symbols) either with single sample method (solid symbol).

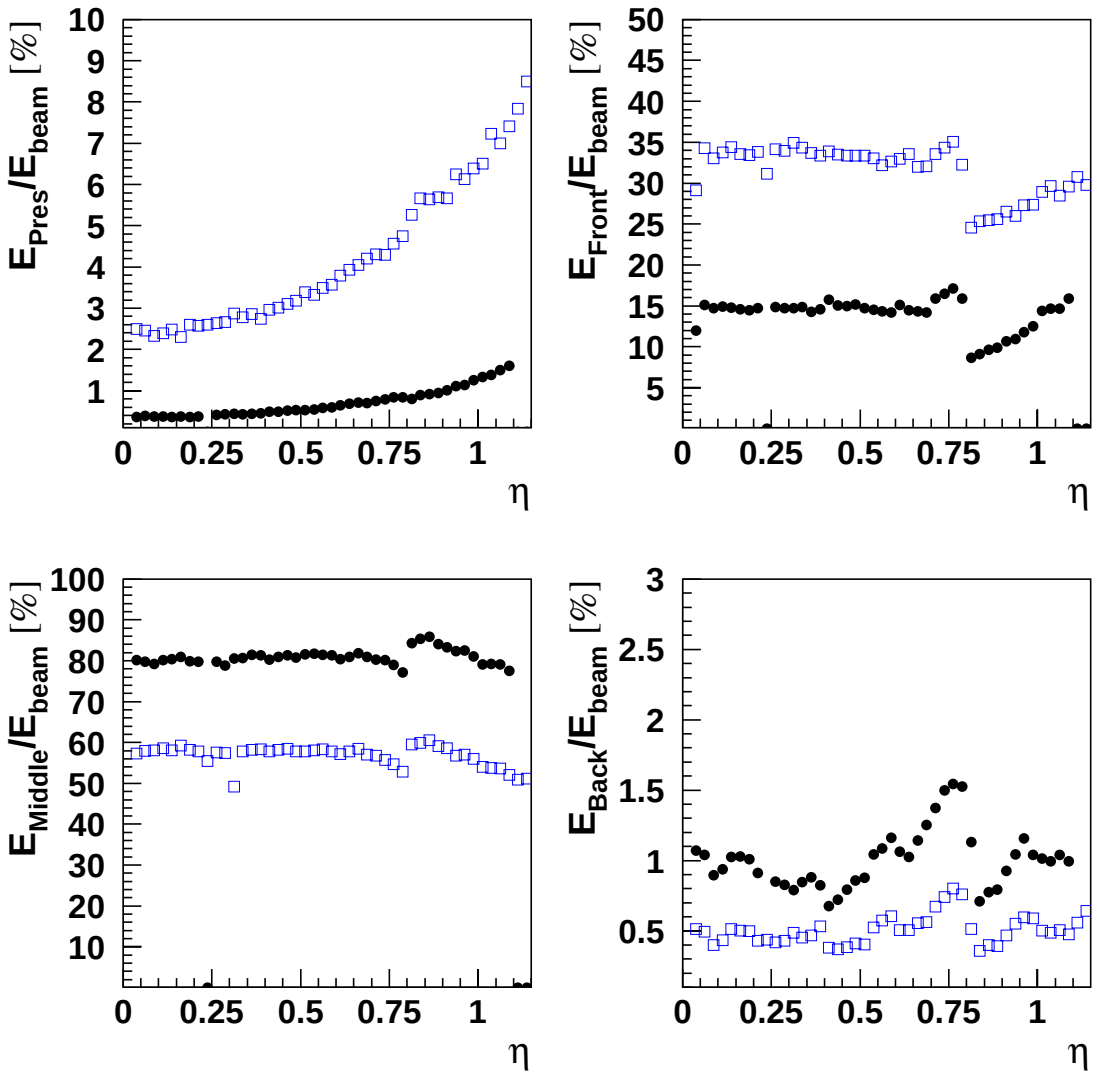

Figure 20: Fraction of energy deposited by electrons in each compartment, as a function of the η coordinate, for incident energies of 245 GeV (full symbols) and 20 GeV (open symbols).

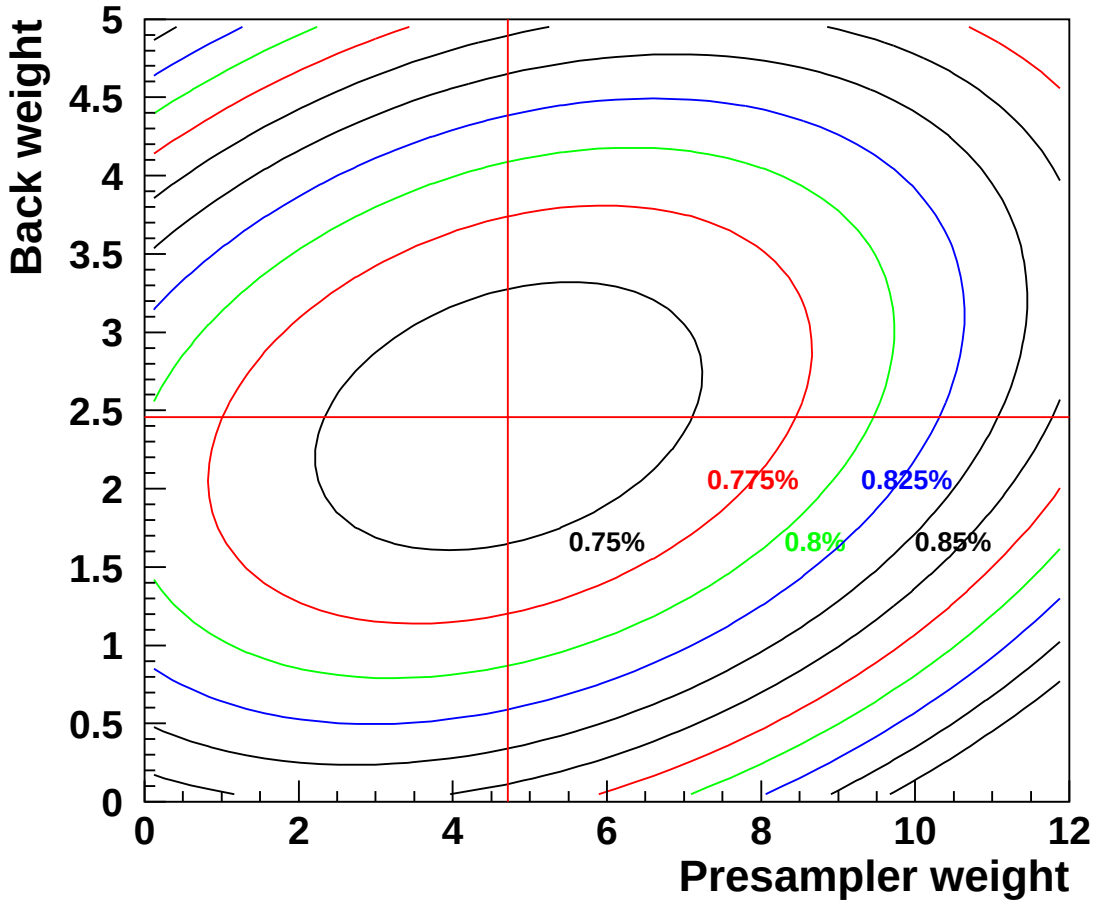

Figure 21: Contour of iso-resolution lines as function of the weight on the presampler and back compartment at $\eta_{Cell} = 15$, $\phi_{Cell} = 10$ for 245 GeV electrons. The best weight combination corresponds to 4.7 (PS) 2.5 (Back) with $\sigma/E = 0.73\%$.

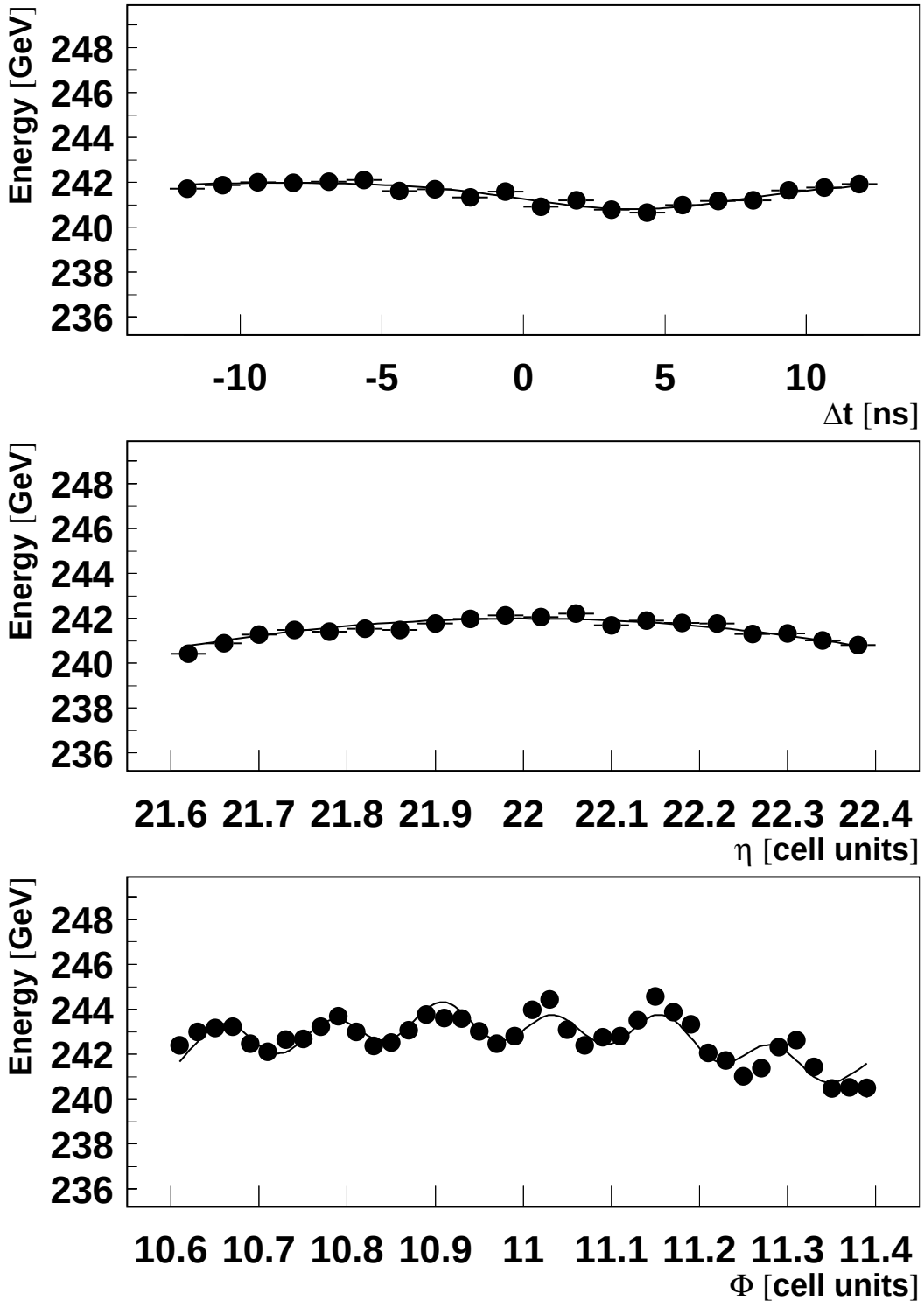

Figure 22: Calorimeter response variation as a function of the 40 MHz clock phase (top), η_{Cell} (middle) and ϕ_{Cell} (bottom). The curves are the fitted correction functions. The distributions are affected by the additional non-homogeneously distributed material upstream of the calorimeter.

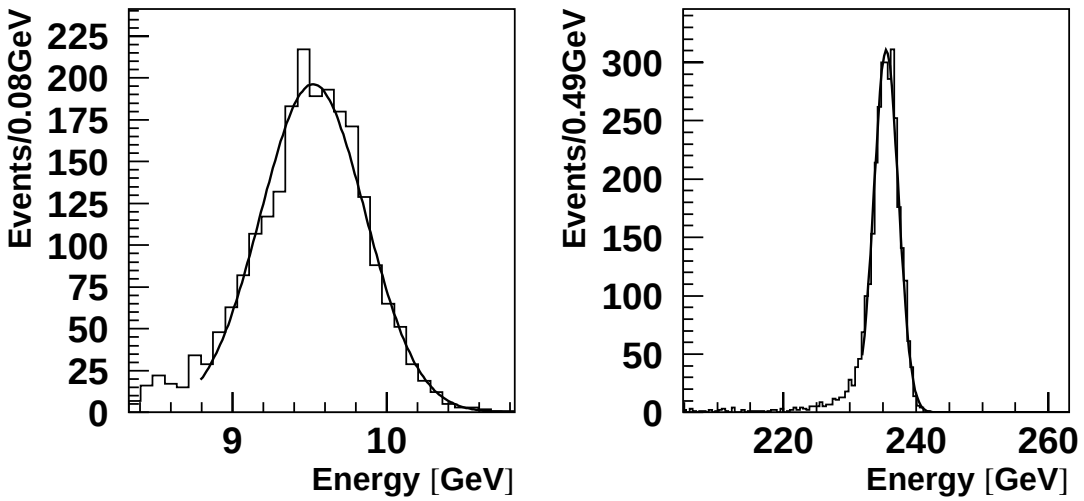

Figure 23: Calorimeter energy response to electrons incident at $\eta_{Cell} = 3$ and $\phi_{Cell} = 10$ and with nominal energies of 10 and 245 GeV. The full line is the result of a Gaussian fit to the distribution.

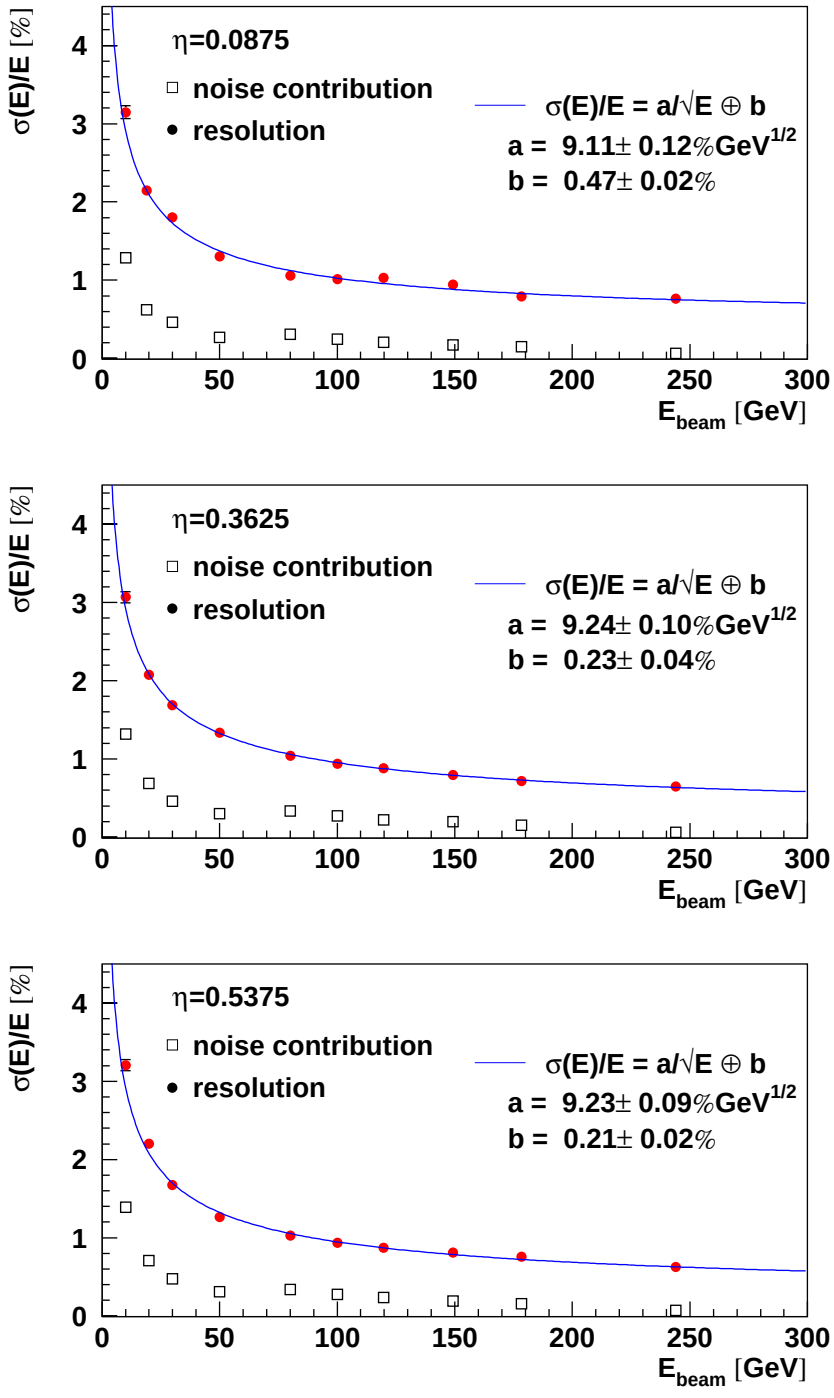

Figure 24: Energy resolution as a function of the electron beam energy at $\eta_{Cell} = 3$, 14, 21 and $\phi_{Cell} = 10$. The full line is the result of the fit to the data. The noise contribution has been subtracted from the resolution.

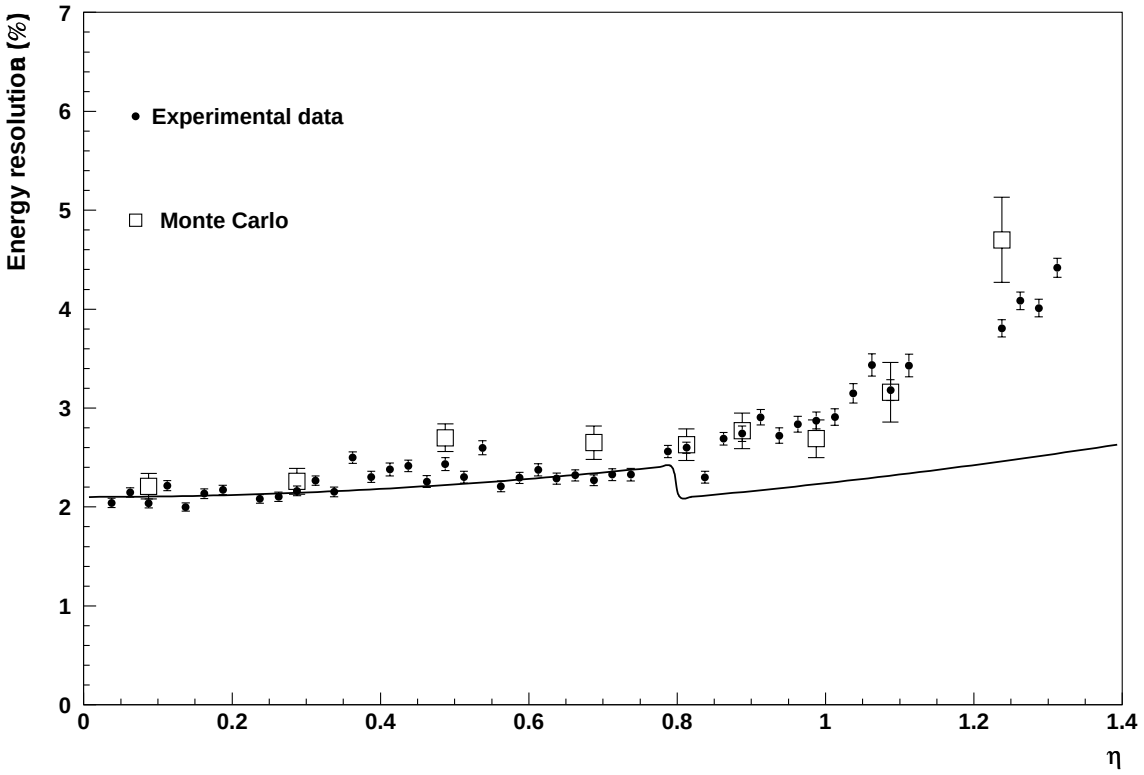

Figure 25: Energy resolution as a function of rapidity, as obtained with an electron beam of 20 GeV. The curve shows the geometrical expectation, normalized at $\eta = 0$ and rescaled at $\eta = 0.8$ with the square root of the ratio of the two lead thicknesses.

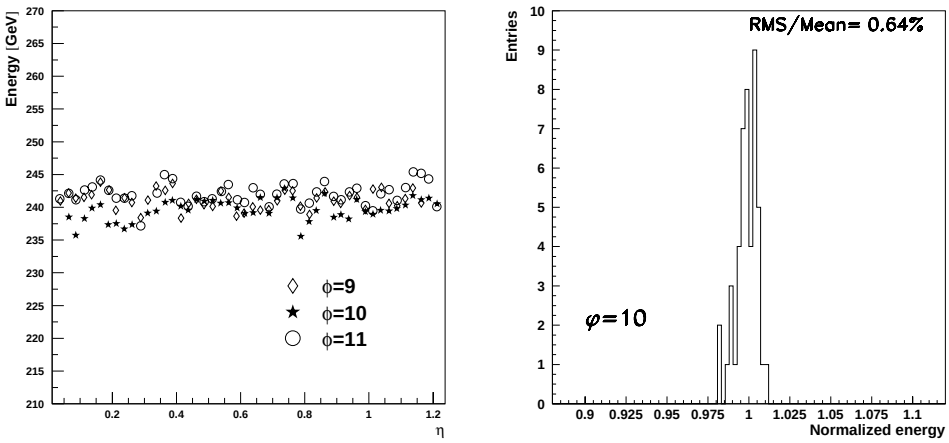

Figure 26: Left: Peak energy response, as a function of the hit cell position in η, as obtained with 245 GeV electrons at three different ϕ. Right: dispersion of the normalized calorimeter response for the 48 η-cells scanned at ϕ=10.

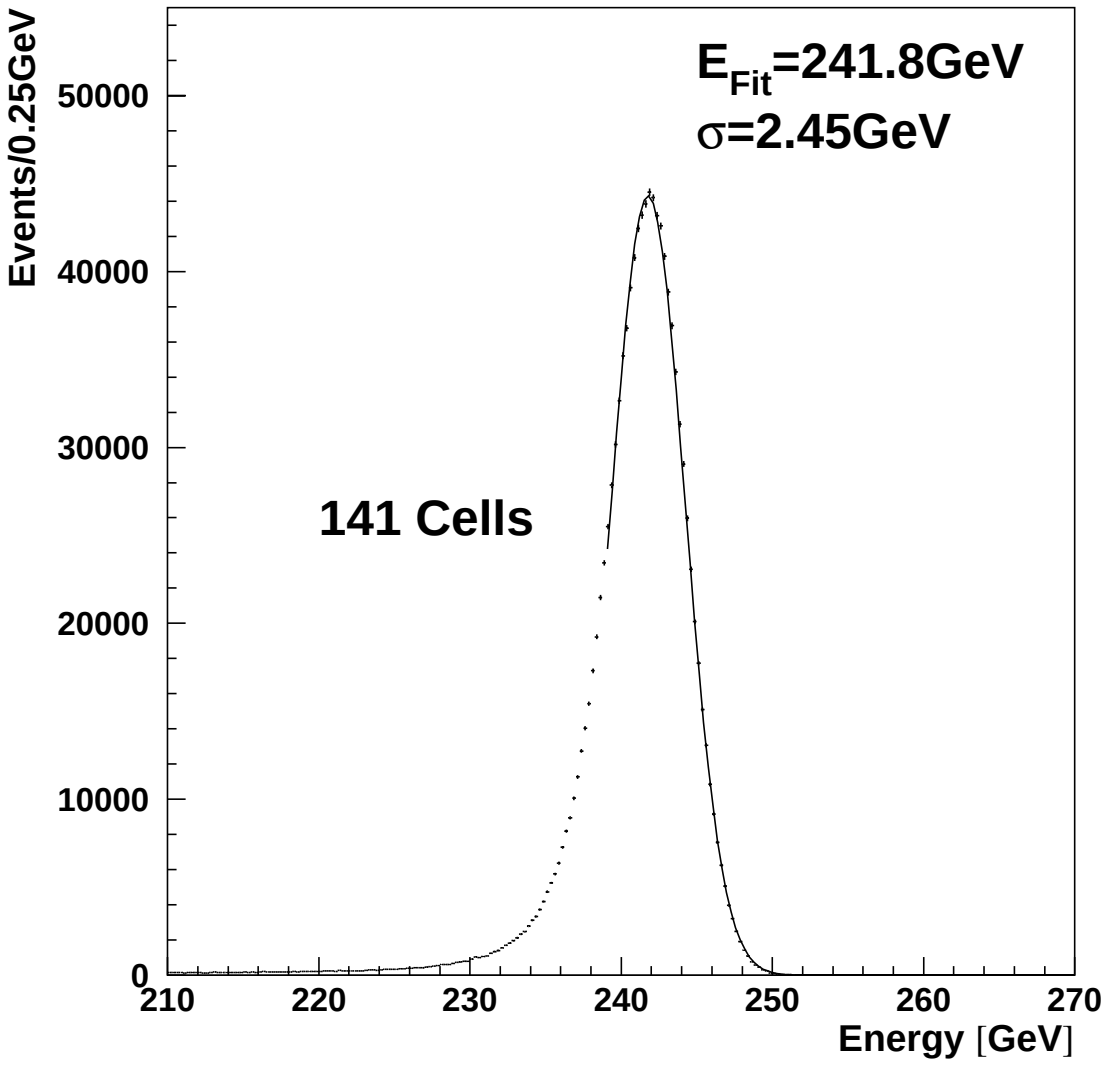

Figure 27: Overall energy spectrum reconstructed in the calorimeter for 245 GeV electrons hitting an area corresponding to 141 middle cells. The result of a Gaussian fit is shown.